Vorticity recirculation and asymmetric generation at a small headland with broadband currents

Michael Kovatch[1], Falk Feddersen[1], Derek Grimes[1], Jamie MacMahan[2]

[1]Scripps Institution of Oceanography, University of California, San Diego, La Jolla, California, USA
[2]Department of Oceanography, Naval Postgraduate School, Monterey, California, USA

Key Points:

- At a 1 km scale headland (Pt. Sal CA), depth averaged vorticity varied $\pm 8f$ and was asymmetrically related to along-headland flow.
- Vorticity also depends on flow acceleration, indicating short (2 h) adjustment timescale, recirculation, and headland generation.
- Estimated potential vorticity across the headland indicates asymmetric vorticity generation stronger for northward flow.

Corresponding author: Michael Kovatch, `mkovatch@ucsd.edu`

Abstract

Fixed ADCP velocity measurements are used to investigate headland vorticity generation and recirculation in $\sim$ 20 m depth around the small ($\sim$ 1 km) central California headland Pt. Sal. To reduce vorticity estimation noise, velocities are reconstructed from the first two EOF modes representing $\approx 73\%$ of the variance. Using fixed ADCPs, depth-averaged vorticity is estimated west and south of Pt. Sal. Only one west-location vorticity component is estimated, leading to negative vorticity bias for northward flow. The south location vorticity is consistent with estimates from parallel vessel transects on one day. The observed depth-averaged flow V was primarily along-bathymetric contours and varied ± 0.2 m s^{-1} across subtidal and tidal frequency bands. The depth-averaged normalized vorticity $\bar{\zeta}/f$ varied ± 8 across all frequency bands. Vorticity distributions are skewed with opposite sign at west and south locations, and $\bar{\zeta}/f < -1$ is more likely at the west location. At both locations, depth-averaged vorticity and velocity are inversely related, with relationship asymmetric with sign of V, indicating headland and farther upstream vorticity generation. Binned-mean $\bar{\zeta}/f$ depends on both V and its time-derivative, and indicates vorticity recirculation across the headland. The $\sim$ 2 h vorticity adjustment timescale and the associated short excursion distances indicate vorticity generation between south and west locations. Potential vorticity changes across the headland are different for positive and negative V indicating headland asymmetric vorticity generation. Pt. Sal occupies a non-dimensional parameter space that is unique relative to other well studied headlands.

1 Introduction

Steady and tidal (oscillating) flows past topographic features such as headlands and islands lead to wake development and eddy shedding (*e.g.,* Signell & Geyer, 1991; Canals et al., 2009; MacKinnon et al., 2019), frontal development from flow separation (Farmer et al., 2002), and internal lee wave generation (*e.g.,* MacCready & Pawlak, 2001; Warner & MacCready, 2014; Voet et al., 2020). Strong relative vorticity ζ was observed for headland and island wakes with ζ/f of $O(1-10)$ (f is the Coriolis parameter) over a range of length-scales, from $O(0.1-10$ km) (*e.g.,* Wolanski et al., 1984; Canals et al., 2009; MacKinnon et al., 2019). Headland and island wakes can be important in the cross-shelf transport of larvae, sediment, and other tracers (*e.g.,* Roughan et al., 2005; George et al., 2015).

Previous modeling studies of wakes generated by steady flow around headlands and islands have mainly focused on obstructions with length-scales L of $O(10$ km), such as Pts. Arena and Reyes (Gan & Allen, 2002). For such headland length-scales, modeled wakes can extend significant distances downstream relative to the length-scale of the headland or island (Gan & Allen, 2002; Dong et al., 2007). Neglecting barotropic or baroclinic tides, about one third of Southern California Bight modeled eddy activity was attributed to island wakes (Dong & McWilliams, 2007). Large scale ($L \sim 10$ km) features and moderate flow rates ($U \sim 0.1\ \mathrm{m\,s^{-1}}$) generally result in a small Rossby number Ro $(= U/fL)$ of $O(0.1)$. Stratification affects headland wakes and is quantified by the Burger number $\mathrm{Bu} = (L_d/L)$, where the baroclinic deformation radius $L_d = Nh/f$ for water depth h and buoyancy frequency N $(= \sqrt{(-g/\rho_0)\rho_z}$, where ρ is density and z is the vertical coordinate). Vorticity generation increases with the Rossby number Ro and, for intermediate Ro and Bu, decreases for increasing Bu (Castelao & Barth, 2006; Dong et al., 2007). The Ro dependence implies that, for a fixed headland and stratification, headland-generated vertical vorticity magnitude $|\zeta|/f$ depends on $|U|$ for steady flow but with vorticity and velocity having opposite signs as flow magnitude is reduced in shallower water where friction is larger.

Other headland wake studies have focused on tidal (*i.e.,* oscillatory) flow. For tidal-flow, vertical vorticity generation has been observed downstream of a headland (*e.g.,* Geyer & Signell, 1990). In a seminal paper, Signell & Geyer (1991) modeled unstratified tidal flow past a symmetric (Gaussian) headland to study the vorticity generation and evolution. The curl of the quadratic bottom stress is key to vorticity generation and dissipation, with a bottom-friction decay scale $t_{\mathrm{bf}} = h/C_D U_0$ based on water depth h, drag coefficient C_D, and tidal velocity U_0. Vorticity evolution depended on three non-dimensional parameters. The first nondimensional parameter is the headland aspect ratio (cross-shore to alongshore extent). Second, the frictional Reynolds number $\mathrm{Re_f} = h/C_D L$ is the ratio between advection and quadratic bottom friction, and represents the vorticity decay length-scale relative to the headland scale L. Third, the Keulegan-Carpenter number $K_c = U_0/\omega L$, where ω is the tidal frequency, is the ratio of tidal excursion amplitude to the headland length-scale. Note, Signell & Geyer (1991) kept the tidal Rossby number U_0/fL fixed, also likely an important parameter. A fourth non-dimensional parameter, based on the others, is the ratio of frictional to tidal time-scale $\omega t_{\mathrm{bf}} = \mathrm{Re_f}/K_c$, which measures whether vorticity is short- ($\mathrm{Re_f}/K_c \ll 1$) or long-lived ($\mathrm{Re_f}/K_c \gg 1$) relative to a tidal cycle. Note, $\mathrm{Re_f}/K_c$ also can be interpreted as the ratio of frictional to tidal length-scales. For $\mathrm{Re_f}/K_c > 1$, the longer-lived vorticity can recirculate back across the headland as the tidal cycle switches, a situation which is not possible for steady flows (finite $\mathrm{Re_f}$ and $\mathrm{Re_f}/K_c \ll 1$). Laboratory experiments of oscillating shallow water flow past a cylinder have enumerated the rich wake behavior over a large range of $\mathrm{Re_f}$ and K_c (*e.g.,* Lloyd et al., 2001). Tidal headland wake eddies were studied on a beach-nourishment generated (Stive et al., 2013) sandy headland with $L \sim 1000$ m, $h \sim 10$ m, and low aspect ratio. In both observations and models, significant but unspecified vorticity was generated every flood tide (Radermacher et al., 2017) with eddy intensity modulated by the spring-neap cycle. These eddies were short-lived (*i.e.,* less than a tidal cycle), suggesting $\mathrm{Re_f}/K_c \lesssim 1$.

Baroclinic effects of tidal flows past $L \sim 1$ km headlands with large aspect ratio in deep water ($h \approx 200$ m) have been studied at the largely symmetric Three Tree Point (TTP, located in the Puget Sound) both with observations and models (Pawlak et al., 2003; Edwards et al., 2004; McCabe et al., 2006; Canals et al., 2009; Warner & MacCready, 2014). As with $L \sim 1$ km scale barotropic headland studies, observed TTP ζ/f is often relatively large, of $O(1)$. TTP vorticity is regularly tilted with respect to stratification (Canals et al., 2009) and short lived relative to the barotropic frictional decay scale t_{bf}, suggesting baroclinic mechanisms associated with tilted vorticity are significant in eddy decay (Pawlak et al., 2003). The baroclinic Froude number $\mathrm{Fr} = U_0/Nd$, with N and obstruction height d, is an additional important nondimensional parameter relevant for both steady (*e.g.,* Dong et al., 2007) and oscillating (*e.g.,* MacCready & Pawlak,

2001) baroclinic wakes. For Fr $\ll$ 1, flow travels around the obstacle, leading to flow separation and potentially eddy formation. As Fr $\approx$ 1, flow transitions to going over the obstacle and can lead to lee wave generation (MacCready & Pawlak, 2001). As part of the Flow Encountering Abrupt Topography (FLEAT) experiment, wake processes around the island of Palau have been extensively studied (MacKinnon et al., 2019; Zeiden et al., 2019; Rudnick et al., 2019; Johnston et al., 2019; Merrifield et al., 2019; Voet et al., 2020). The Palau bathymetry is deep with large aspect ratio, similar to TTP, but with larger ($L \sim 10$ km) "headland" scale. Regional currents have both tidal, near-inertial, and lower frequency variability. Flows past the steep regional bathymetry can generate both nonlinear internal lee waves (Voet et al., 2020) and large-scale, high Ro vorticity, suggesting significant variability in Fr (Rudnick et al., 2019; MacKinnon et al., 2019; Zeiden et al., 2019).

Most locations cannot be neatly classified into pure steady or tidal flow, and instead have broadband flows, comprised of low frequency subtidal (time-scale $>$ 33 h) plus tidal (diurnal and semidiurnal) flows of comparable magnitude. Vorticity generation with broadband flows is different from steady or oscillating flow alone (MacKinnon et al., 2019). For example, under combined strong steady and weak tidal flow, a series of same-signed vortices are likely generated and advected downstream. Aside from MacKinnon et al. (2019), most headland studies are for either oscillatory (tidal) or (quasi-) steady flow. Whether a steady-flow type relationship between local velocity and vorticity applies in broadband flows is unknown. For steady flows, headland flow response is different for symmetric and asymmetric obstacle (Castelao & Barth, 2006). Previously studied headlands at $L \sim 1$ km scale are also either largely symmetric (TTP) or have small aspect ratio (Zandmotor). Most modeling and laboratory studies use symmetric obstacles. In many cases, in particular on the US West Coast, headlands are asymmetric to the alongcoast flow, which may result in vorticity generation that is asymmetric with flow direction. These aspects of shallow small asymmetric headlands have not previously been studied. Lastly, strong anticyclonic vorticity $\zeta/f < -1$ will be centrifugally unstable (*e.g.,* Hoskins, 1974) and has low probability in open ocean observations and models (*e.g.,* Shcherbina et al., 2013a). However, the likelihood of strong anticyclonic versus cyclonic vorticity near a vorticity generating headland has not previously been studied.

Headland wake generation is naturally studied with vertical vorticity ζ. Whereas vorticity is straightforwardly estimated from numerical model solutions of headland or island wake flows (*e.g.,* Signell & Geyer, 1991), it is challenging to estimate observationally. Headland estimated vorticity used either shipboard ADCP surveys (Geyer & Signell, 1990; Pawlak et al., 2003; Canals et al., 2009; MacKinnon et al., 2019) or drifters (Pawlak et al., 2003). Yet, these studies were limited to measurements over, at most, a few semidiurnal cycles. To study headland vorticity generation with broadbanded currents, long vorticity timeseries that include subtidal and spring-neap tidal variability are required. This requires vorticity time-series estimated from fixed current meters, which has not previously been reported. Such longer-term vorticity observations at a headland under broadband currents can address the questions above and others such as: Is vorticity generated at a headland or is it advected from farther upstream? How much recirculation of vorticity occurs as along-headland flow switches sign?

Here, we address these headland vorticity related questions with a two-month (fall 2017) time-series of vorticity estimated at two locations across Pt. Sal, a small $O(1$ km) asymmetric headland with $O(1)$ aspect ratio located on the central California coast (Fig. 1), during the Inner-shelf Dynamics Experiment (Kumar et al., 2020). This region often has a headland wake as illustrated with a long-wave infrared (LWIR) surface temperature and ADCP-measured flow (*e.g.,* Figure 1) with cool water (blue/green colors) streaming off Pt. Sal to the south-west and curves to the south-east. This wake orientation is consistent with the observed depth-averaged currents (black arrows). Headland vorticity generation and recirculation are studied statistically with vorticity estimated from fixed ADCP observations at two locations west and south of Pt. Sal. The study site, velocity filtering methods, and vorticity estimation technique are described in section 2. Statistical analysis of depth-averaged velocity and vorticity at the west and south locations in isolation and comparison with vessel-based vorticity are given in section 3. In section 4, the local vorticity and velocity relationship is examined in regards to vorticity generation and recirculation. Potential vorticity in a steady flow paradigm is used to examine asymmetric headland vorticity generation (section 5). In the discussion, the relationship between vorticity recirculation and generation is examined (section 6.1) and Pt. Sal is placed in (dimensional and non-dimensional) context relative to other headlands (section 6.2). Section 7 is a summary.

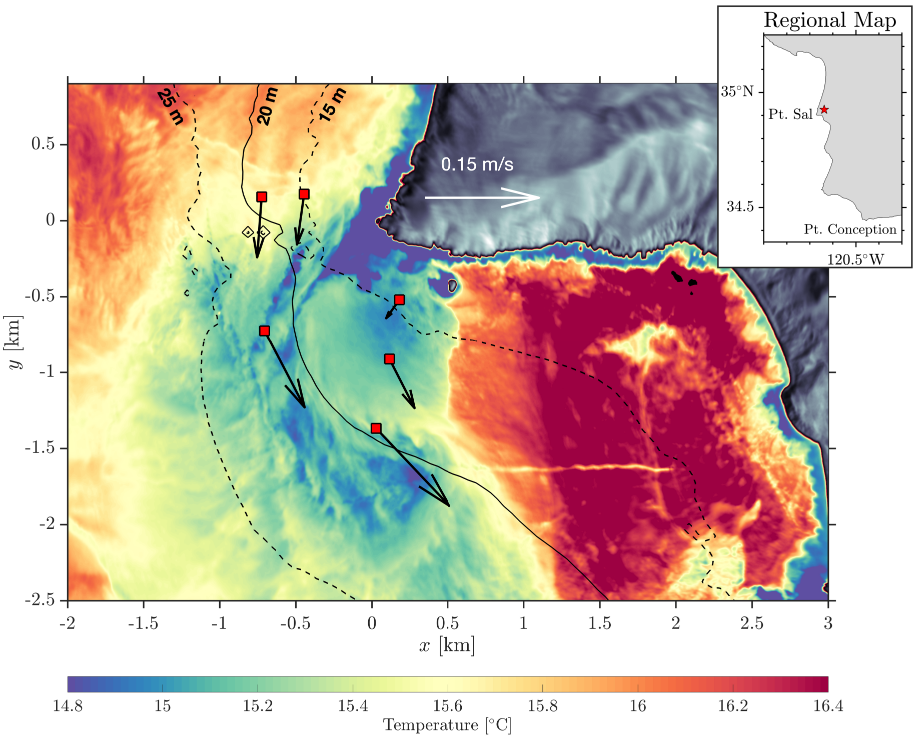

Figure 1. Long-wave infrared (LWIR) map of surface temperature around Pt. Sal, CA from the airborne Modular Aerial Sensing System (MASS, Melville et al., 2016). An Easting (x) and Northing (y) coordinate system is defined with origin at the tip of Pt. Sal (34.9030°N, 120.6721°W). Blue colors are cooler and red colors are warmer. Snapshot taken over a 3-minute window (11-Sep-2017, 10:41-10:44 PDT), overlaid with depth-averaged ADCP velocities (black arrows) which are time-averaged over same duration. The solid and dashed lines represent the 15, 20, and 25 m depth contours. (Inset) Map of Pt. Sal in the context of Pt. Conception.

2 Data and Methods

2.1 Experiment and regional description

In the fall of 2017, multiple institutions participated in the Inner Shelf Dynamics Experiment funded by an Office of Naval Research Departmental Research Initiative (ISDE) (Lerczak et al., 2019; Kumar et al., 2020). The experiment consisted of observations spanning 50 km alongshore on the Central CA coast, centered on the asymmetric rocky headland Pt. Sal (Fig. 1), over Sept to Oct 2017. An Easting (x) and Northing (y) coordinate system is defined with origin $(x, y) = (0, 0)$ m at the tip of Pt. Sal (34.9030°N, 120.6721°W). Northward of the point, the coastline is relatively straight, sandy beach interrupted with another small symmetric headland 3 km to the north. At Pt. Sal, the coast is rocky and the coastline bends approximately 120°. To the west of Pt. Sal, bathymetry contours are relatively compressed close to the point with several shoals and outcrops within 500 m west of the point, evidenced by cold water stream off of them (Fig. 1). From Pt. Sal, the rocky coastline extends eastward for 2.5 km before bending to the south where bathymetry contours are farther from shore and slopes are less steep.

Pt. Sal is located in an upwelling region, and the subtidal large-scale flow is primarily southward with episodic northward warm-water flow due to wind relaxation events, common during the fall months (Melton et al., 2009; Washburn et al., 2011; Suanda et al., 2016; Aristizábal et al., 2017). In addition, barotropic tides drive oscillating currents at Pt. Sal. Furthermore, semidiurnal nonlinear internal waves (NLIWs) regularly propagate into Pt. Sal (Colosi et al., 2018; Kumar et al., 2019; Feddersen et al., 2020), adding complexity. During the experiment, a broad array of 173 moorings and bottom landers were deployed from 100 m to 9 m depth along the 50 km stretch of coastline with many ADCPs, thermistors, and wave buoys in conjunction with multiple coastal high-frequency radars and meteorological stations (Kumar et al., 2020). In addition, two week-long intensive operations periods (IOPs) were conducted, one in mid-September (IOP1) and the other in mid-October (IOP2) with multiple vessels and aircraft sampling concurrently. Here, we only present a small subset of the experiment data that are focused on Pt. Sal. Additional information and studies related to the Inner Shelf Dynamics experiment are Lerczak et al. (2019); Spydell et al. (2019); McSweeney et al. (2020); Feddersen et al. (2020); Kumar et al. (2020).

2.2 Pt. Sal, CA moored and fixed location observations

Here we focus on an array of fixed location (bottom mounted, upward looking) ADCPs (Fig. 1, red squares) and thermistor moorings deployed (not shown) near Pt. Sal from September 1, 2017 through October 19, 2017 in water depths ranging from 13.5 to 25.0 m. This subset of locations was chosen for their high spatial resolution within a few km of the tip of Pt. Sal. Each thermistor mooring had 7–11 RBRsolo T thermistors with 1.5, 2, or 3 m vertical spacing (shallow moorings had higher vertical resolution) and a near bead RBR soloD pressure sensor. RBR soloT's have 0.002°C accuracy, RBR soloD's have 0.01 m accuracy, and both sampled at 1 Hz. Bottom mounted, upward-looking ADCPs measuring profiles of eastward and northward velocity (u, v) were co-located with a subset of the thermistor moorings. Here, z is the vertical coordinate positive upward and $z = 0$ m is the deployment time-averaged mean sea surface.

Most fixed location ADCPs were either 600 kHz or 1 MHz Nortek Aquadopp with vertical bin width Δz of 0.5—1 m. Two ADCPs were five-beam Nortek Signature1000 with $\Delta z = 0.5$ m. All ADCPs also had a pressure sensor used to estimate the tidal sea-surface. ADCP velocity data within 2 m of the tidal sea surface or with low amplitudes or correlations are removed. The lowest ADCP $\Delta z = 1$ m bin varies from 1 m to 2.6 m above the seabed, depending on bin size and blanking distance. The uppermost ADCP bin varies from $z = -3$ m to $z = -4$ m (relative to the mean sea level) due to the ± 1 m tidal range, the large (≈ 2.5 m at times) surface gravity waves, and side-lobe interference. All moored thermistor and ADCP data were averaged to a 1 minute sample interval and time-aligned from 13:00PDT 6-September to 06:00PDT 15-October, and hereafter this time period is denoted the *analysis period*. For fluctuating flows, a low-pass time filter acts as a spatial filter at time-scales less than the dominant tidal velocity time-scale (Lumley & Terray, 1983a). Thus, to reduce aliasing of short length-scale (high horizontal wavenumber) variability in the vorticity calculations, moored ADCP velocities are low-pass filtered with a 2 h cutoff. For reference, this gives a 720 m cutoff length-scale for a steady 0.1 $\mathrm{m\,s^{-1}}$ current. Velocity data are then interpolated onto fixed vertical z levels at $\Delta z = 1$ m intervals, where $z = 0$ m is the mean tidal water level. This allows estimation of horizontal velocity gradients at a particular z level.

2.2.1 Vertical cEOF velocity reconstruction and depth-averaged statistics

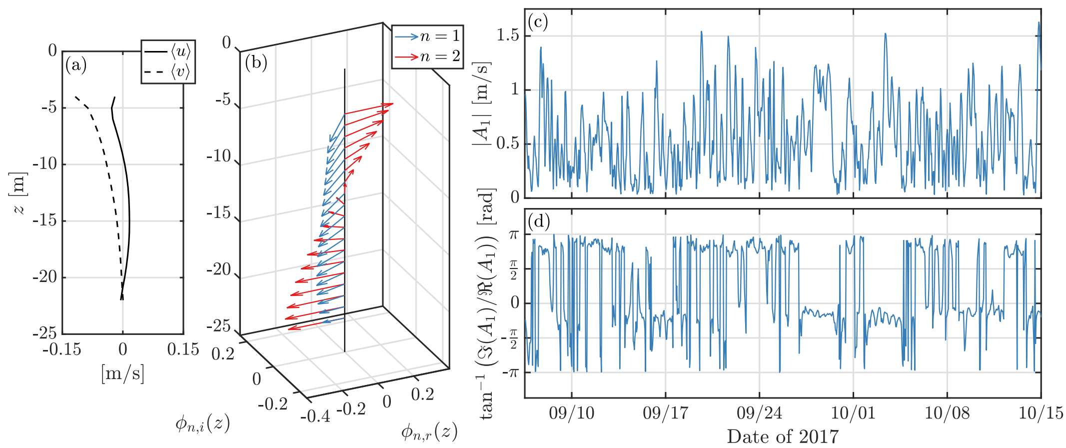

Figure 2. Complex empirical orthogonal function (cEOF) decomposition of (u, v) ADCP velocities at $(x, y) = (-705, -725)$ m: (a) Mean horizontal velocities ($\langle u \rangle$,$\langle v \rangle$) as a function of distance below mean sea level z. (b) Structure of cEOFs mode 1 (ϕ_1, blue) and mode 2 (ϕ_2, red) versus z, (c) first cEOF $|A_1|$ and (d) phase ($\tan^{-1}[\Im(A_1)/\Re(A_1)]$) time series over the analysis period. Mode 1 and mode 2 capture 52% and 21% of velocity variance, respectively.

To further reduce aliasing of short length-scale velocity variability that potentially alias vorticity, the 2-h low-pass filtered ADCP velocities are additionally smoothed by reconstructing velocities from a complex empirical orthogonal function (cEOF) decomposition (*e.g.,* Kundu & Allen, 1976; Kumar et al., 2015). At each moored ADCP, the 2-h low-pass filtered velocities are decomposed into time-mean ($\langle u \rangle$, $\langle v \rangle$, where $\langle\,\rangle$ denotes a time average over the analysis period) and fluctuating (u', v') components (*i.e.,* $u = \langle u \rangle + u'$). The cEOF decomposition is performed on the complex fluctuating velocity,

$$\psi(z, t) = u'(z, t) + \mathrm{i}\, v'(z, t), \qquad (1)$$

where $\mathrm{i} = \sqrt{-1}$. The complex velocity ψ is decomposed into a set of orthogonal modes

$$\psi(z,t) = \sum_{n=1}^{N} \phi_n(z) A_n(t), \tag{2}$$

where $\phi_n(z)$ is the n-th eigenvector (EOF) of the Hermitian covariance matrix of ψ and $A_n(t)$ is the amplitude time series of mode n. Both $\phi_n(z)$ and $A_n(t)$ are complex-valued variables consisting of information related to both $u'(z,t)$ and $v'(z,t)$.

An example cEOF decomposition on a 600 kHz Nortek Aquadopp ADCP located south-west of Pt. Sal at $(x, y) = (-705, -725)$ m and mean depth $h = 25$ m is shown in Figure 2. The northward time-averaged current $\langle v \rangle$ is negative (southward) and surface intensified near 0.12 $\mathrm{m\,s^{-1}}$ and approximately zero near the bed (Fig. 2a, solid). The eastward time-averaged current $\langle u \rangle$ is weak (≈ 0.03 $\mathrm{m\,s^{-1}}$) and offshore (onshore) in the upper (lower) water column (Fig 2b, dashed). The cEOF mode $n = 1$ velocity structure explains 52% of the variance and is mostly barotropic (unidirectional and weakly depth varying) with near-surface velocities veering roughly 45° counterclockwise (blue, Fig. 2b). Time-series analysis indicates that the mode $n = 1$ amplitude magnitude $|A_1|$ is dominated by subtidal and tidal band variability as seen in Fig. 2c. The $A_1(t)$ phase varies bimodally indicating primarily NW to SE flow. The cEOF mode $n = 2$ explains 21% of the variance and has vertical structure that changes sign mid-depth, qualitatively consistent with the first baroclinic mode (red, Fig. 2b). Time-series analysis reveals that the mode $n = 2$ amplitude A_2 (not shown) has more high-frequency variability equally split between super-tidal (> 2.2 cpd) and lower-frequencies (< 2.2 cpd). For cEOF modes $n \geq 3$ (not shown), the variance percentage captured diminishes quickly, the modes are comprised of high vertical wavenumber variability, and the corresponding amplitudes are dominated by supertidal > 2.2 cpd variability.

This cEOF decomposition framework is applied to the ADCPs deployed near Pt. Sal. At each of these ADCPs, a smoothed velocity is reconstructed using only the first two cEOF modes, *e.g.,*

$$u(z,t) = \langle u \rangle + \Re\left[\sum_{n=1}^{2} \phi_n(z) A_n(t)\right] \tag{3a}$$

$$v(z,t) = \langle v \rangle + \Im\left[\sum_{n=1}^{2} \phi_n(z) A_n(t)\right] \tag{3b}$$

where $\Re$ and $\Im$ indicate the real and imaginary components, respectively. This reconstructed velocity captures 73%±5% of the variance at the 9 ADCPs presented in Fig. 4. Hereafter, $u(z,t)$ and $v(z,t)$ represent the 2-h low-pass filtered and cEOF (3) reconstructed ADCP velocities and will be used in subsequent analysis. Excluding higher cEOF modes removes high frequency (higher horizontal wavenumber) and high vertical wavenumber noise, giving a smoothed velocity signal for estimating vorticity.

At each ADCP, depth-averaged velocities (denoted with capitals, *i.e.,* $[U(t), V(t)]$) are calculated by vertically averaging $(u(z,t), v(z,t))$ velocity over the vertical range of valid observations for the entire analysis period. For example, the vertical range for the ADCP in Fig. 2 is $z = -21$ m to $z = -4$ m. No extrapolation to the free surface or the bed is performed as it relies on assumptions regarding the surface and bottom boundary layer which may bias the depth-average. Depth-averaged velocity variance major and minor axis and orientation are calculated (*e.g.,* Emery & Thomson, 2001) from an eigenvalue decomposition of the (U, V) velocity variance and covariances (e.g. $\langle U'^2 \rangle$, $\langle U'V' \rangle$) yielding principal axis angle θ_p, major axis U^2_{maj} and minor axis U^2_{min} variances, allowing for plotting of velocity standard deviation ellipses (analogous to tidal ellipses). The

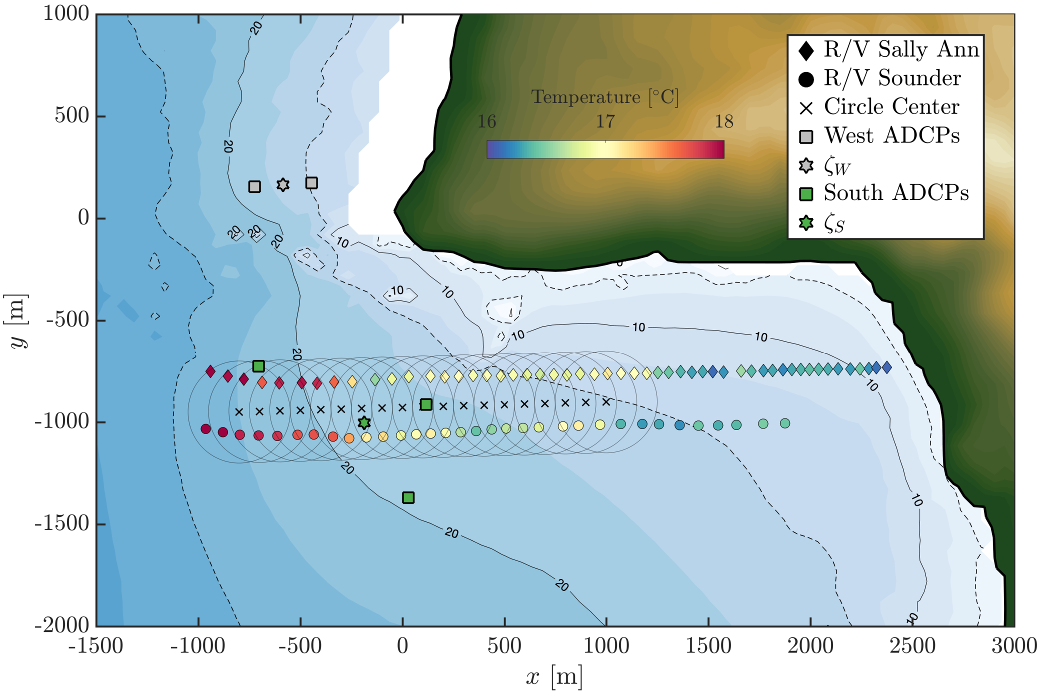

Figure 3. Map of mooring- and vessel-based vorticity estimation locations near Pt. Sal as a function of x and y with local bathymetry. West vorticity ζ_W (gray star) is estimated from west ADCPs (gray squares). South vorticity ζ_S (green star) is estimated at centroid of south ADCP triangle (green squares). For reference, a pair of simultaneous parallel vessel tracks for the *R/V Sally Ann* (colored diamonds) and *R/V Sounder* (colored circles) are shown. Colors represent vessel transect near-surface temperature ($z = -1.5$ m) from CTD observations. Data shown are from September 13, 2017, 10:54-11:19 PDT (later denoted as transect 3) and are representative of all transects. For each vessel transect, vessel-based vorticity is estimated at black "x"s (100 m separation) using vessel ADCP observations within the 250 m radius circles (gray).

variances (e.g. $\langle U'^2 \rangle$) include variability over subtidal, tidal, and supertidal frequency bands. Velocity and vorticity variables are decomposed using the PL64 filter (Limeburner et al., 1985) into subtidal (< 0.73 cpd), diurnal (0.73–1.5 cpd), semi-diurnal (1.5–2.2 cpd) and supertidal (2.4 cpd to 12 cpd) frequency band components. Statistics (means and standard deviations) are calculated for each of these frequency band components.

2.2.2 Fixed ADCP vorticity estimation

Estimating ocean vertical vorticity $\zeta = v_x - u_y$ is inherently difficult as two-dimensional spatial differences of noisy velocity observations are required. Vorticity has been estimated via many methods, including drifters (*e.g.,* Pawlak et al., 2003; Ohlmann et al., 2017; Spydell et al., 2019), radar (*e.g.,* Kirincich, 2016), gliders (*e.g.,* Zeiden et al., 2019), and vessels transects (*e.g.,* Geyer & Signell, 1990; Rudnick, 2001; Pawlak et al., 2003; Shcherbina et al., 2013b; MacKinnon et al., 2019). To reduce noise in the estimated spatial velocity derivatives from fixed-ADCPs motivates the use of the 2-h filtered and cEOF reconstructed ADCP velocity time-series. Using the moored ADCP velocities (3), vertical vorticity ζ is estimated at two locations near Pt. Sal (Fig. 3, green and gray stars). Vorticity at the "south" location $\zeta_{\mathrm{S}}(z,t)$ ($[x,y]=[-187,-1003]$ m), is estimated with three ADCPs in a triangular configuration (green squares in Fig. 3) via plane fit to the 2-h low pass and cEOF reconstructed moored ADCP (u,v) velocities. Specifically, (u,v) are fit to the functions

$$u_i(z,t) = u_{\mathrm{S}} + \frac{\partial u}{\partial x}(x_i - x_{\mathrm{S}}) + \frac{\partial u}{\partial y}(y_i - y_{\mathrm{S}}), \tag{4a}$$

$$v_i(z,t) = v_{\mathrm{S}} + \frac{\partial v}{\partial x}(x_i - x_{\mathrm{S}}) + \frac{\partial v}{\partial y}(y_i - y_{\mathrm{S}}), \tag{4b}$$

where i represents the ADCP number, (x_S, y_S) is the centroid of the "south" triangle, (u_S, v_S) are centroid fit velocities, $\partial(u,v)/\partial x$ and $\partial(u,v)/\partial y$ are the fit velocity gradients (*e.g.,* Molinari & Kirwan, 1975). The base and height of the triangle (or its edges) are 464 m and 842 m. This fit is performed for the vertical levels $z=-18$ m to $z=-4$ m which are present at all 3 ADCPs. This plane fitting method assumes (u,v) vary linearly in both x and y between the mooring locations. With three ADCPs, the fit is exact and any ADCP noise or small-scale (u,v) variability will alias noise into the estimated velocity gradient. The use of the 2-h low pass filtering and the cEOF velocity reconstruction reduces the ADCP noise and small-scale spatial (u,v) variability, resulting in reduced estimated velocity gradient noise. The velocity gradients calculated from plane fitting should be interpreted as being constrained to scales on the order of the ADCP separation (≈ 1 km) and longer, as shorter scale vorticity variability is not resolved. From the resulting fit parameters, "south" vorticity at the centroid location (green star, Fig. 3) is estimated as

$$\zeta_{\mathrm{S}}(z,t) = \frac{\partial v}{\partial x} - \frac{\partial u}{\partial y}. \tag{5}$$

At the location just west of Pt. Sal, "west" vorticity $\zeta_W(z,t)$ ($[x,y]=[-585,165]$ m) is estimated from two ADCPs in a line extending west off of the point (Fig. 3, gray star and squares). With only two locations, the plane fit method (5) cannot be used and only a single vorticity component is estimated analogous to single underway ADCP transects (*e.g.,* Rudnick, 2001; Zeiden et al., 2019). Here, the 2-h low-pass filtered and cEOF reconstructed velocities are rotated into an "alongshore" coordinate system $(\tilde{u},\tilde{v})$ that is $4.91°$ east of north, an average of the two ADCP principal axes (Fig. 4). At every 1 m from $z=-15$ to -4 m where both moorings always had valid data, "west" vorticity $\zeta_W(z,t)$ is estimated as the cross-shore gradient ($\Delta\tilde{x}=276$ m) of rotated alongshore velocity between the two moorings (*i.e.,* $\partial\tilde{v}/\partial\tilde{x}$), neglecting the $\partial\tilde{u}/\partial\tilde{y}$ term. This assumption is likely reasonable as the upstream velocity is locally alongshore uniform (*i.e.,* $\partial\tilde{u}/\partial\tilde{y}\approx 0$). This also assumes that alongshore velocity varies linearly with $\tilde{x}$ constraining the scale of vorticity to the ≈ 300 m ADCP separation scale. However, for northward flow, $\partial\tilde{u}/\partial\tilde{y}$ could be significant due to flow separation and recirculation west and north of Pt. Sal, resulting in an incomplete ζ_W estimate. For analysis purposes, the west vorticity ζ_{W} estimate is used for both southward and northward flow conditions. The potential bias in ζ_{W} for southward and northward flow is discussed in Appendix A.

In addition to vorticity, the centroid velocities at the south (*i.e.,* (u_S,v_S) in Eq. 4) and west (u_W,v_W) locations are depth averaged over the z-range where the ADCPs used in the fit had valid data and rotated into their principal axes directions ($44.3°$ west of north and $4.9°$ east of north). These principal axes are nearly the average of the individual moored ADCP principal axes (Figure 4). The depth-averaged principal axes alongshore velocities are denoted as V_{S} and V_{W}, respectively, and will be used in subsequent analysis.

2.3 Vessel-based observations and vorticity estimates

Here, coordinated vessel-based parallel transects from SIO's *R/V Sally Ann* and UW-APL's *R/V Sounder* from IOP1 on 13 September were used to estimate both vorticity components as in Shcherbina et al. (2013b). Both vessels performed tow-yo CTD casts using RBR Concerto CTDs sampling at 6 Hz (Sally Ann) or 12 Hz (Sounder) with an accuracy of 0.002°C. Data from each cast are filtered with half-power cutoff of 0.25 m and vertically gridded to 0.1 m resolution. Each vessel also was equipped with a pole-mounted, downward-looking TeleDyne RDI WorkHorse ADCP capable of bottom tracking. *R/V Sally Ann* had a RDI 300 kHz ADCP with 1 m vertical bins and 1 s sampling intervals while *R/V Sounder* had a RDI 1200 kHz ADCP with 1 m bins and 3 s sampling intervals. Note the 18 m profiling range is within the RDI 1200 kHz ADCP manufacturer's upper limit. ADCP data for both vessels were averaged down to 1 minute. During transects the *R/V Sally Ann* and *R/V Sounder* vessel speeds were approximately 1 $\mathrm{m\,s^{-1}}$ and 1.7 $\mathrm{m\,s^{-1}}$, respectively. This yielded average ADCP spatial resolution of 62 m and 102 m, respectively and average CTD cast spatial resolution of 65 m and 89 m, respectively.

On 13 September, three repeated west to east parallel transects were conducted south of Pt. Sal by *R/Vs Sally Ann* and *Sounder*, intersecting the triangle used to calculate ζ_{S} (Figure 3). These parallel transects occurred during southward flow in the lee of Pt. Sal and were north-south separated by approximately 250–300 m (Figure 3). The 10:54–11:19 PDT transect provides an example of the surface temperature structure in the lee of Pt. Sal. Near-surface temperature varied from warm (near 18°C) farther offshore to cold (near 16°C) within the bay on both transects (Figure 3). A $\Delta T \approx 1$°C temperature front is evident between $-500 < x < 0$ m, near the south vorticity centroid location (green star in Figure 3). Vessel-based temperature transects are estimated by averaging CTD temperature between the *R/V Sally Ann* and *Sounder*. If one vessel is missing data, the average is not calculated. As CTD casts were not full water-column depth, temperature is estimated over the upper 2/3 of the water column.

Vessel-based vorticity $\zeta_{\mathrm{V}}(x, z)$ is calculated at the center of the two parallel transects from $-1000 \leq x \leq 1000$ m at 100 m intervals (see "x" in Figure 3) At each "x" location, all vessel-based (u, v) data that fall within a search circle of radius $R = 250$ m are used to least-squares plane-fit velocity gradients (*i.e.,* Eq. 4) at particular z levels. Velocity gradients are estimated from $-20.5 \leq z \leq -2.5$ m at 1 m intervals. Best-fits are removed when circles have fewer than 5 data points or when observations are time-separated by more than 15 min, to minimize aliasing from temporal and spatial misalignment in vessel sampling. Vorticity at each "x" is then estimated from the best-fit velocity gradients, which then provides a spatial map of $\zeta_{\mathrm{V}}(x, z)$ for each transect. This process is repeated for the three parallel transects conducted on this day.

3 Spatial structure and temporal variability of vorticity estimates

3.1 Fixed-location depth-averaged velocity statistics near Pt. Sal

Before examining vorticity, we first examine the depth-averaged (barotropic) velocity statistics within a few km of Pt. Sal (Figure 4) to provide context about the barotropic flow around the headland. Depth-averaged velocity means and standard deviation ellipses (analogous to tidal ellipses) are calculated over the analysis period (13:00PDT 6-Sept to 06:00PDT 15-Oct) and standard deviations include variability over subtidal, tidal, and supertidal frequency bands. For $y > 0$ m (west and north of Pt. Sal), the time-

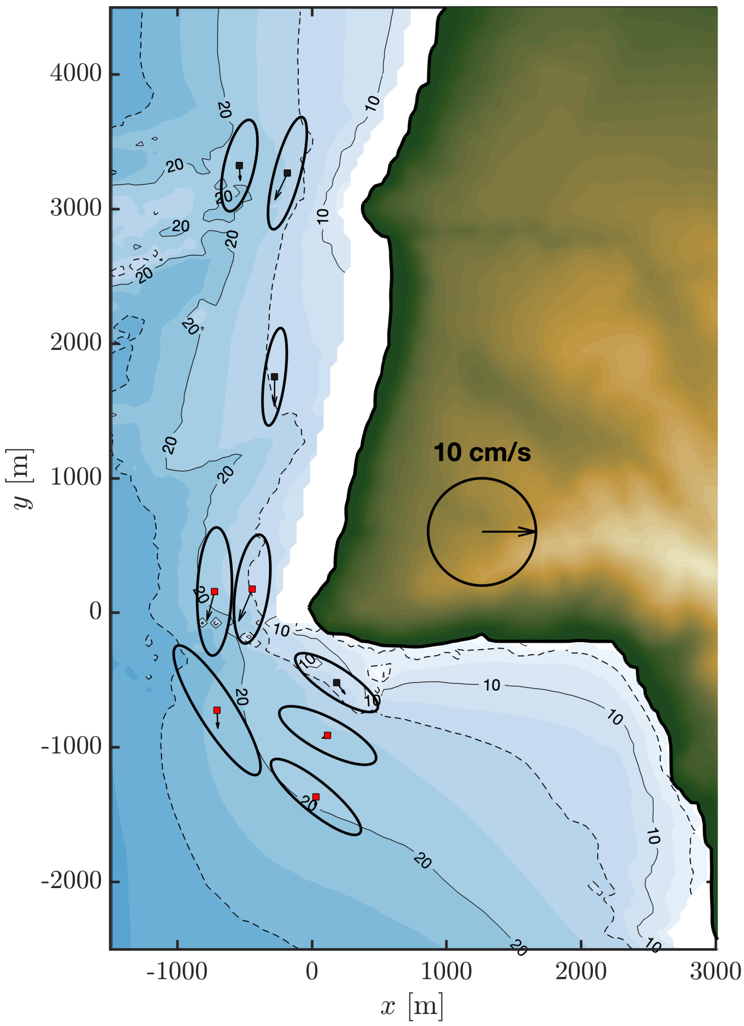

Figure 4. Fixed-location ADCP depth-averaged velocity time-means (arrow) and standard deviation ellipses (black ellipse) as a function of x and y near Pt. Sal. Ellipses have major and minor axes as U_{maj} and U_{min} and orientation angle θ_p, and are analogous to tidal ellipses but include all frequency bands. Time-averaging is over the analysis period (13:00PDT 6-Sept to 06:00PDT 15-Oct). Solid contours are 10 and 20 m isobaths with dashed contours denoting 5 m intervals. White denotes regions without bathymetry data.

mean (over the analysis period) and depth-averaged velocities are largely southward and along-isobath with magnitudes of 0.03–0.05 $\mathrm{m\,s^{-1}}$ (arrows in Figure 4). For $y < 0$ m (south of Pt. Sal), the time-mean depth-averaged velocities are weaker (0.01–0.02 $\mathrm{m\,s^{-1}}$) with variable directions. Over all ADCPs the principal (major) axis velocity standard deviation (*i.e.*, U_{maj}) varies between 0.09–0.14 $\mathrm{m\,s^{-1}}$ (ellipses in Figure 4), substantially larger than the mean flow, and is largely oriented along-isobath. Depth-averaged current variability is strongly polarized with minor to major axis standard deviation $U_{\mathrm{min}}/U_{\mathrm{maj}}$ between 0.2–0.3. The depth-averaged current variability is roughly comprised of equal subtidal and tidal (diurnal and semidiurnal) variability.

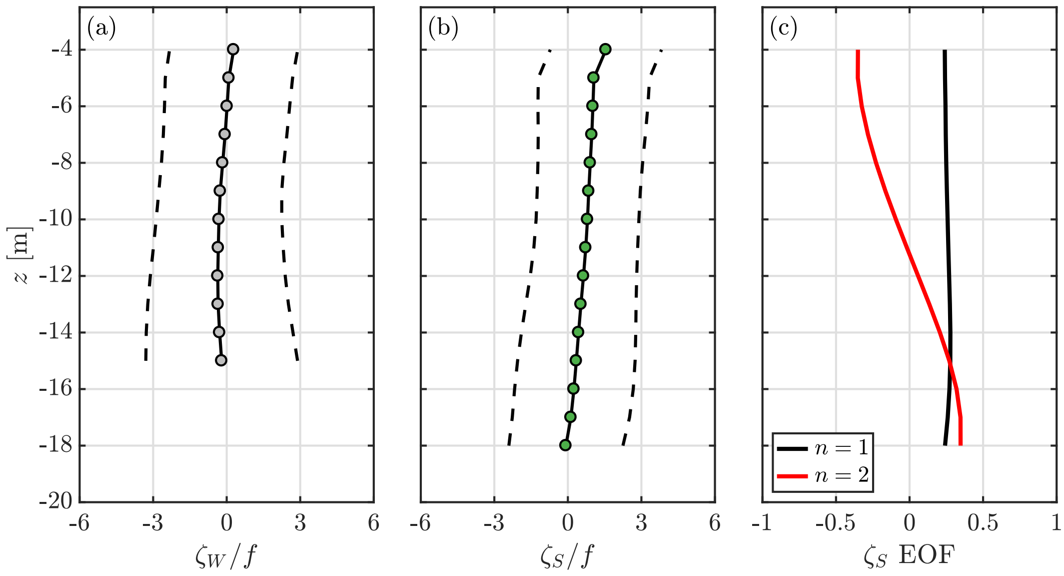

Figure 5. Time-mean (solid) and standard deviation (dashed) of normalized vorticity ζ/f versus depth z at the (a) west ζ_W and (b) south ζ_S locations (Figure 3). (c) South vorticity ζ_S EOF modes 1 and 2 versus z, representing 64% and 27% of variability, respectively. Statistics are calculated over the analysis period (13:00PDT 6-Sept to 06:00PDT 15-Oct).

The relative orientation of the velocity standard deviation ellipses reveals aspects relevant to vorticity (Figure 4). For example, near the small headland (Mussel Rock, $y \approx$ 3000 m), southward flow velocities are generally stronger closer to shore likely due to the very rough bathymetry (denoted rocky outcrop in Colosi et al., 2018) enhancing drag near the offshore ADCP. In contrast, just west of Pt. Sal (red squares west of Pt. Sal, Figure 4), southward flow velocities are generally weaker in shallower water. South of Pt. Sal, velocity ellipses rotate to the southeast quasi-following bathymetry contours. The ADCPs used for south vorticity (ζ_S) all have different ellipse orientations demonstrating presence of non-zero depth-averaged vorticity.

3.2 Fixed-location vorticity

Here, we examine the vertical structure of the two fixed-location vorticity estimates (ζ_W and ζ_S) and subsequently the time-variability of the depth-averaged vorticity in the context of barotropic tide and depth-averaged along-headland velocity. The time means and standard deviations (over the analysis period, 13:00PDT 6-Sept to 06:00PDT 15-Oct) of ζ_W and ζ_S vertical structure are shown in (Figure 5a,b). For all analyses, vorticity is normalized by the local inertial frequency $f = 8.34 \times 10^{-5}$ s^{-1}. At the western location (Figure 5a), time-mean vorticity $\langle\zeta_W\rangle/f$ is near zero throughout the water column with largely vertically uniform standard deviations of approximately ± 3. At the southern location (Figure 5b), mean vorticity $\langle\zeta_S\rangle/f$ increases with z, from near-zero close to the bed to $1.6f$ near-surface. The ζ_S standard deviation (std) is slightly weaker near ≈ 2.25 and slightly more depth uniform than ζ_W. Note, the west location vorticity statistics are potentially biased for northward flow (Appendix A).

Although the vertical structure of vorticity variability is largely depth uniform (Figure 5a,b), the vertical coherence of said variability is examined with a vertical EOF de-

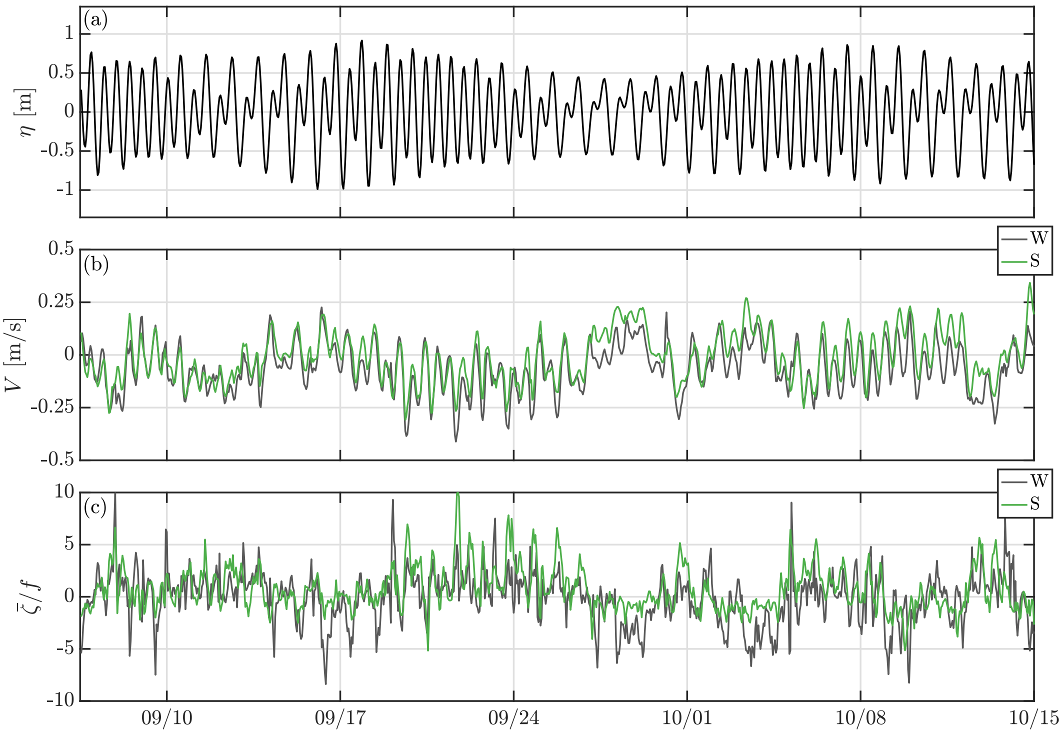

Figure 6. Time-series of (a) tidal elevation η, (b) depth-averaged centroid principal axes alongshore velocity V, and (c) normalized depth-averaged vorticity $\bar{\zeta}/f$. In (b,c), gray and green correspond to west and south locations, respectively. In panels (b,c), The correlation between V_{S} and V_{W} is $r = 0.86$ and between $\bar{\zeta}_{\mathrm{S}}/f$ and $\bar{\zeta}_{\mathrm{W}}/f$ is $r = 0.55$.

composition on both ζ_{S} and ζ_{W}. The 1st EOF mode for ζ_{S} (black line) is strongly barotropic and captures 64% of the vorticity variance whereas the 2nd EOF mode (red line) has a mode-1 baroclinic structure accounting for 27% of variance (Figure 5c). Both EOF modes 1 and 2 for ζ_W are similar to those for ζ_S in both vertical structure (not shown) and variance fraction (65% and 27%, respectively). The vertically smooth ζ/f means and low mode dominance of ζ/f variability indicates that the vorticity estimation method using 2-h filtered and cEOF reconstructed velocities (Section 2.2.1) is not noise contaminated due to aliasing of short scale variability associated with internal warm bores or solitons (Colosi et al., 2018; McSweeney et al., 2020) that likely have contributions at cEOF mode 2. If noise were significant, one would expect small-scale vertical variation in the statistics due to estimation error. That the temporal ζ variability is largely depth-uniform also indicates that the depth-averaged vorticity can be used to study the vorticity kinematics and dynamics. Here, the depth-averaged vorticity is denoted with an overbar (*i.e.,* $\bar{\zeta}_S$) and as with depth-averaged V is the average over the vertical range where vorticity could be estimated. Subsequent analyses are conducted with depth-averaged, normalized vorticity $\bar{\zeta}/f$.

The time-series of tidal elevation η, depth-averaged centroid principal-axes alongshore velocity $(V_{\mathrm{S}}, V_{\mathrm{W}})$, and depth-averaged vorticity $(\bar{\zeta}_{\mathrm{S}}/f, \bar{\zeta}_{\mathrm{W}}/f)$ are used to to examine the time-scales of variability of each and the similarities and differences between the west and south locations. Recall, that velocity and vorticity variables are decomposed into subtidal, diurnal, semidiurnal, and supertidal components from which statistics are

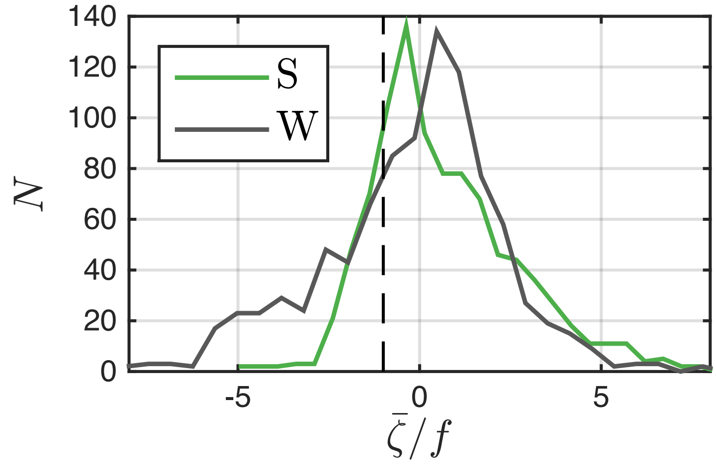

Figure 7. Histogram of south $\bar{\zeta}_{\mathrm{S}}/f$ (green) and west $\bar{\zeta}_{\mathrm{W}}/f$ (gray) normalized vorticity. The vertical dashed line represents $\bar{\zeta}/f = -1$ or zero potential vorticity. The vorticity $\bar{\zeta}_{\mathrm{S}}/f$ skewness is 0.88, significantly elevated over $\bar{\zeta}_{\mathrm{W}}/f$ skewness of -0.19. Note that $\bar{\zeta}_{\mathrm{S}}/f < -1$ and $\bar{\zeta}_{\mathrm{W}}/f < -1$ (*i.e.,* left of the dashed line) for 19% and 31% of the time, respectively.

calculated (Section 2.2.1). The analysis period (13:00PDT 6-Sept to 06:00PDT 15-Oct) spanned nearly 3 spring-neap tidal cycles (Figure 6a), with spring tides of ± 1 m and neap tides of ± 0.5 m. The depth-averaged V_{S} and V_{W} vary largely from ± 0.2 m s^{-1} with (semidiurnal and diurnal) tidal and subtidal variability (Figure 6b). At the west location, the time mean flow is southward ($\langle V_{\mathrm{W}} \rangle = -0.06$ m s^{-1}), but near-zero at the south location ($\langle V_{\mathrm{S}} \rangle = 0.01$ m s^{-1}). The V_{S} and V_{W} have similar std (≈ 0.12 m s^{-1}) and are well correlated ($r = 0.86$) across the tidal and subtidal time-scales. At the south location, subtidal variability is dominant with velocity amplitude (not std) of 0.13 m s^{-1}. Semidiurnal variability is second largest with spring neap velocity amplitude varies from 0.03–0.1 m s^{-1}. The west location is similar. The depth-averaged $\bar{\zeta}_{\mathrm{S}}/f$ and $\bar{\zeta}_{\mathrm{W}}/f$ vary ± 8 with subtidal, tidal, and more high-frequency variability than V (Figure 6c). The time mean south vorticity $\langle \bar{\zeta}_{\mathrm{S}}/f \rangle = 0.7$ is elevated relative to the west vorticity $\langle \bar{\zeta}_{\mathrm{W}}/f \rangle = 0.2$. In contrast, the west location std$(\bar{\zeta}_{\mathrm{W}}/f) = 2.5$ is elevated compared to std$(\bar{\zeta}_{\mathrm{S}}/f) = 2.1$, consistent with the vorticity standard deviations over the vertical (Figure 5a,b). Relative to velocity, the elevated high frequency vorticity variability is expected as the higher horizontal wavenumbers of vorticity correspond to higher frequencies in steady and oscillatory flows (Lumley & Terray, 1983b). The west and south vorticity is less correlated ($r = 0.55$) than for V, which may be due to vorticity generation between the two locations or west-location vorticity bias (Appendix A).

Histograms of south ($\bar{\zeta}_{\mathrm{S}}/f$) and west ($\bar{\zeta}_{\mathrm{W}}/f$) vorticity reveal differences between the two locations (Figure 7). The $\bar{\zeta}_{\mathrm{S}}/f$ distribution is highly skewed around the mean $\langle \bar{\zeta}_{\mathrm{S}}/f \rangle = 0.7$, with much higher probability of large positive than negative $\bar{\zeta}_{\mathrm{S}}/f$ (green curve in Figure 7). The skewness $\langle (\bar{\zeta}'_{\mathrm{S}}/f)^3 \rangle / \langle (\bar{\zeta}'_{\mathrm{S}}/f)^2 \rangle^{3/2} = 0.88$ is strongly positive and only infrequently (19%) is the south location potential vorticity negative (*i.e.,* $\bar{\zeta}_{\mathrm{S}}/f < -1$, left of dashed line in Figure 7). Such strong positive skewness is qualitatively consistent with Gulf Stream vorticity observations on similar spatial scales (Shcherbina et al., 2013a). In contrast, the $\bar{\zeta}_{\mathrm{W}}/f$ distribution (gray curve in Figure 7) is much more symmetric around mean $\langle \bar{\zeta}_{\mathrm{W}}/f \rangle = 0.2$, with smaller and opposite signed skewness of

-0.19. The west location potential vorticity is negative ($\bar{\zeta}_{\mathrm{W}}/f < -1$) 31% of the time, much more frequently than for $\bar{\zeta}_{\mathrm{S}}/f$. Velocity skewness at V_{S} is 0.22 and for V_{W} is -0.11, much less pronounced than vorticity skewness but with similar signs. The differences in the vorticity distributions are also evident in the time-series (Figure 6c). Away from boundaries and surface or bottom forcing, strong anticyclonic flows ($\bar{\zeta}/f < -1$) are unstable (*e.g.,* Hoskins, 1974) and are thus less likely. For example, Shcherbina et al. (2013a) observe Gulf Stream near-surface $\zeta/f < -1$ about 5% of the time. In contrast, the enhanced likelihood of $\bar{\zeta}/f < -1$ at the west (31%) and south (19%) locations indicates strong vorticity generation effects. This will be examined further in Section 5. As discussed in Appendix A, northward flow may bias the negative $\bar{\zeta}_{\mathrm{W}}/f$ magnitude low.

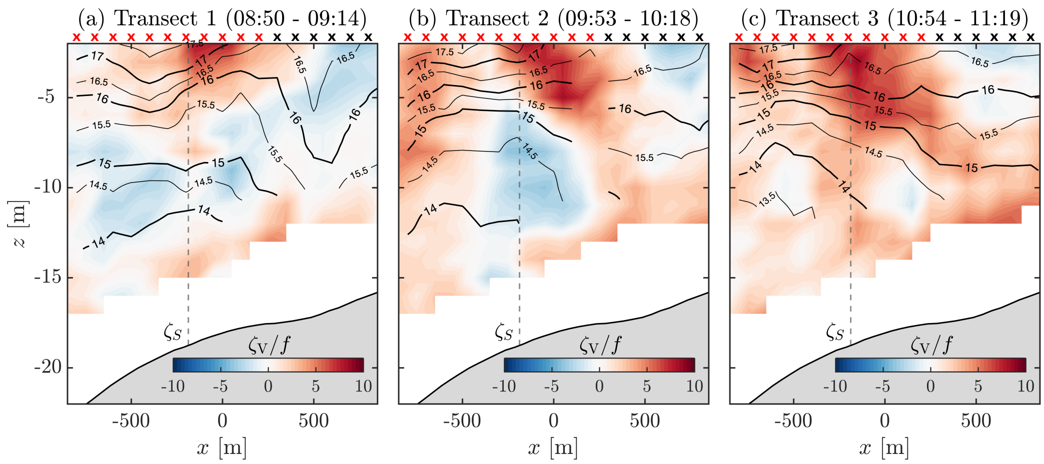

Figure 8. Normalized vessel-based vorticity ζ_{V}/f (color) sections as a function of x and z with overlaid vessel-averaged averaged temperature T (solid black lines) for transects (a) 1 (08:50-9:14), (b) 2 (09:53-10:18), and (c) 3 (10:54-11:19). The x location of ζ_{S} is indicated by the vertical dashed line. Bathymetry is shown in gray. The 'x's above each panel represent locations where vorticity is estimated, and red 'x's represent locations within the triangle used to estimate $\bar{\zeta}_{\mathrm{S}}/f$.

3.3 Vessel-based vorticity

Next, we examine vorticity variability at short time-scales (few hours) and relatively short length-scales (100–1000 m) using three vessel-based vorticity and temperature transects (Section 2.3) shown in Figure 8. Recall, these vessel observations are based on 1-min averages (60–100 m spatial scales) and are essentially snapshots relative to the 2-h low-pass filtered and cEOF reconstructed fixed ADCP observations. In transect 1 (08:50–09:14, Figure 8a), near surface ($z > -5$ m) ζ_{V}/f is largely positive near $+2$ for $x < 500$ m with a 400 m-wide elevated patch $\zeta_{\mathrm{V}}/f \approx 8$ near $x = 0$ m. In an intermediate layer ($-12 < z < -5$ m), $\zeta_{\mathrm{V}}/f \approx -2$ is largely negative and surface outcrops for $x > 500$ m, associated with near-surface colder water (*e.g.,* Figure 3) and an isotherm trough at $x \approx 500$ m. In the region for $x < 200$ m, the stratification is relatively weak with a roughly $\Delta z = 6$ m separation between the 15°C and 17°C isotherms. Near bed ($z < -12$ m), $\zeta_{\mathrm{V}}/f \approx 2$ is largely positive.

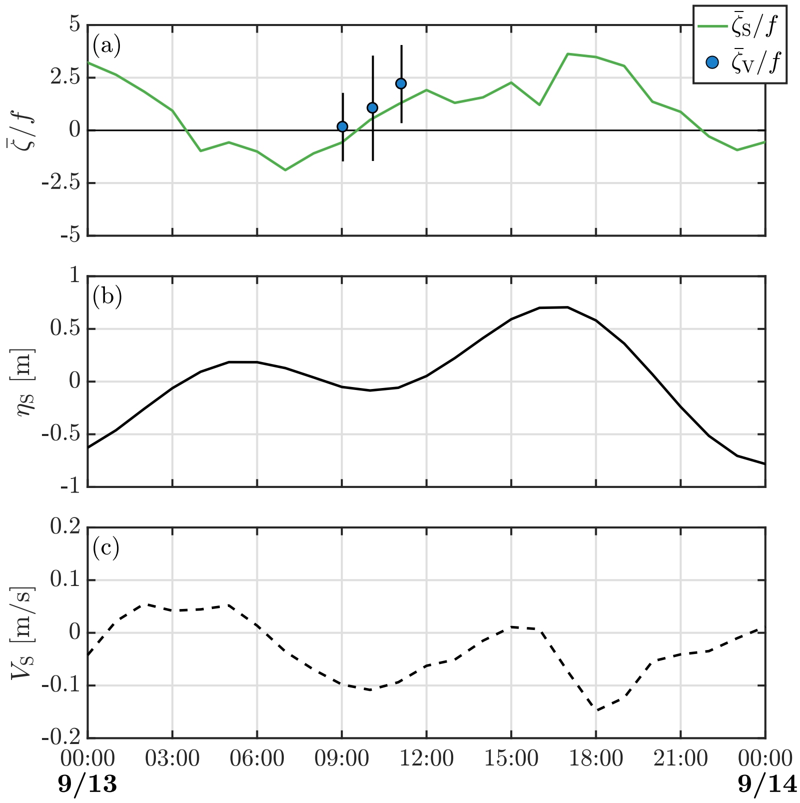

Figure 9. (a) Time-series of 13-Sept south-location hourly depth-averaged vorticity $\bar{\zeta}_S/f$ (green line) and concurrent vessel transect-averaged vorticity $\bar{\zeta}_V/f$ (blue circles). Transect-averaged $\bar{\zeta}_V/f$ is vertically averaged from near-bed to $z = -4.5$ m and cross-shore averaged from $x = -800$ m to 200 m. The blue circle is located at the transect mid-point time and the circle width represents the transect duration. Vertical bars on circles are the standard deviation of ζ_V/f over the averaging region. (b) Hourly tidal elevation η_S (black, solid) and (c) depth-averaged principal axis velocity V_S (black, dashed) 13-Sept time series from the southern vorticity estimate location.

With later transects, vorticity mostly increases and the 15°C and 17°C isotherms tilt downward and upward onshore, respectively (Figure 8b,c). In the near-surface ($z > -5$ m) of transect 2 (09:53–10:18, Figure 8b), two strong positive ζ_V/f patches are present. The $x \approx 0$ m patch from transect 1 has become larger with maximum $\zeta_V/f \approx 8$, and a second patch near $x = -700$ m is evident at $\zeta_V/f \approx 5$. Small negative ζ_V/f is seen near-surface for $x > 500$ m and subsurface near $x = -200$ m. The isotherm tilting has increased upper-water column stratification at $x = -500$ m. In transect 3 (10:54–11:19, 8c), ζ_V/f continues to increase and is positive almost everywhere for $x < 300$ m. The near-surface $\zeta_V/f \approx 8$ patch at $x \approx 0$ m is much larger, but near-surface weak negative ζ_V/f persists onshore $x > 500$ m. The tilting of the 15°C and 17°C isotherms has increased, further increasing the upper-water column stratification near $x = -500$ m.

3.4 Inter-comparison between fixed- and vessel-based vorticity

Here, we inter-compare the fixed- ($\bar{\zeta}_{\mathrm{S}}/f$) and vessel-based ($\bar{\zeta}_{\mathrm{V}}/f$) vorticity estimates (Figure 9). For each vessel transect, a mean (depth- and cross-shore averaged) vorticity $\bar{\zeta}_{\mathrm{V}}/f$ is estimated from the transect $\zeta_{\mathrm{V}}(x,z)$ (Figure 8) by vertically averaging from the near-bed to $z=-4.5$ m and cross-shore averaging from $x=-800$ m to $x=200$ m (indicated with red 'x' in Figure 8). The vertical and horizontal averaging ranges are chosen to be consistent with the depth coverage and horizontal scale of the fixed ADCPs used to estimate $\bar{\zeta}_{\mathrm{S}}/f$ (Figure 3). The standard deviation of ζ_{V}/f is also similarly estimated. The time of the transect-averaged $\bar{\zeta}_{\mathrm{V}}/f$ is the median time of the $x=-800$ to $x=200$ m portion of the transect. No additional filtering of ζ_{V}/f is performed, contrasting with the 2-h low-pass filtered and cEOF reconstructed fixed ADCP velocities.

Over the 24 h of 13 Sept, the fixed $\bar{\zeta}_{\mathrm{S}}/f$ varied quasi-diurnally from roughly -2 to 3 (Figure 9a). The barotropic tide was mixed diurnal and semi-diurnal with about 1.2 m range (Figure 9b). The depth-averaged south velocity V_{S} was largely negative with semidiurnal fluctuations between -0.1 to 0 $\mathrm{m\,s^{-1}}$ (Figure 9c). During the transect time period (08:50–11:19), $\bar{\zeta}_{\mathrm{S}}/f$ increased quasi linearly from near 0 to 2, as the tide underwent an ebb to flood transition. The time period of the transects corresponded to maximal southward flow $V_{\mathrm{S}}=-0.1$ $\mathrm{m\,s^{-1}}$ with a transition from weak negative to positive acceleration.

The three discrete vessel vorticity $\bar{\zeta}_{\mathrm{V}}/f$ estimates are similar to $\bar{\zeta}_{\mathrm{S}}/f$ with same increasing vorticity trend and the fixed $\bar{\zeta}_{\mathrm{S}}/f$ are always within <0.4 standard deviations of $\bar{\zeta}_{\mathrm{V}}/f$ (Figure 9a). This suggests that $\bar{\zeta}_{\mathrm{V}}/f$ is biased high relative to $\bar{\zeta}_{\mathrm{S}}/f$ with average error of ≈ 0.5, but that otherwise these vorticity estimates are robust. The elevated $\bar{\zeta}_{\mathrm{V}}/f$ bias may be because the vessel vorticity $\zeta_{\mathrm{V}}(x,z)$ is estimated on smaller length-scales (*i.e.,* a search radius of 250 m), whereas $\bar{\zeta}_{\mathrm{S}}/f$ is estimated over a scale of ≈ 1000 m using time- and vertical smoothed velocities (Section 2.2.1). Thus, $\zeta_{\mathrm{V}}(x,z)$ contains more high horizontal wavenumber variability (for example, see the 400 m wide $\zeta_{\mathrm{V}}/f>5$ patch in Figure 8b). Alternatively, negatively biased $\bar{\zeta}_{\mathrm{S}}/f$ (relative to ζ_{V}/f) may result from weak near bottom vorticity ($-18<z<-14$ m, Figure 5b), whereas ζ_{V} is on average estimated only to $z\approx-15$ m (Figure 8). Overall, the $\bar{\zeta}_{\mathrm{S}}/f$ and $\bar{\zeta}_{\mathrm{V}}/f$ similarity indicates robust depth-averaged vorticity estimates and provides confidence in subsequent analysis using $\bar{\zeta}_{\mathrm{S}}/f$.

4 Local Vorticity and Velocity Relationship

Based on steady flow Rossby number dependence (*e.g.,* Castelao & Barth, 2006; Dong et al., 2007), the near-headland vorticity is expected to be negatively related to the along-headland flow. For time-dependent (reversing) flows, vorticity can also recirculate around a headland (*e.g.,* Signell & Geyer, 1991). Here, we examine the hourly $\bar{\zeta}_{\mathrm{S}}/f$ and $\bar{\zeta}_{\mathrm{W}}/f$ vorticity dependence on the local major-axis depth-average velocity (V_{S} and V_W) and its time-derivative at both south and west locations (Figure 10). At the south location, $\bar{\zeta}_{\mathrm{S}}/f$ is generally positive for southward flow ($V_{\mathrm{S}}<0$), and negative for northward flow ($V_{\mathrm{S}}>0$) with squared correlation $r^2=0.42$ (Figure 10a). This negative-signed vorticity-velocity relationship is expected in a steady flow paradigm. The binned-mean $\bar{\zeta}_{\mathrm{S}}/f$ and V_{S} relationship is tighter ($r^2=0.94$), and highlights an asymmetry in slope that depends on the V_{S} sign. For $V_{\mathrm{S}}<0$ (*i.e.,* $\bar{\zeta}_{\mathrm{S}}/f$ in the lee of Pt. Sal) the resulting $\bar{\zeta}_{\mathrm{S}}/f$ magnitude (*i.e.,* $\approx$ 3.8 for $V_{\mathrm{S}}=-0.2$ $\mathrm{m\,s^{-1}}$) is larger than for $V_{\mathrm{S}}>0$ when located upstream of Pt. Sal (*i.e.,* $\bar{\zeta}_{\mathrm{S}}/f\approx-1.5$ for $V_{\mathrm{S}}=0.2$ $\mathrm{m\,s^{-1}}$). This asymmetry is consistent with vorticity generation at the headland or farther upstream. The

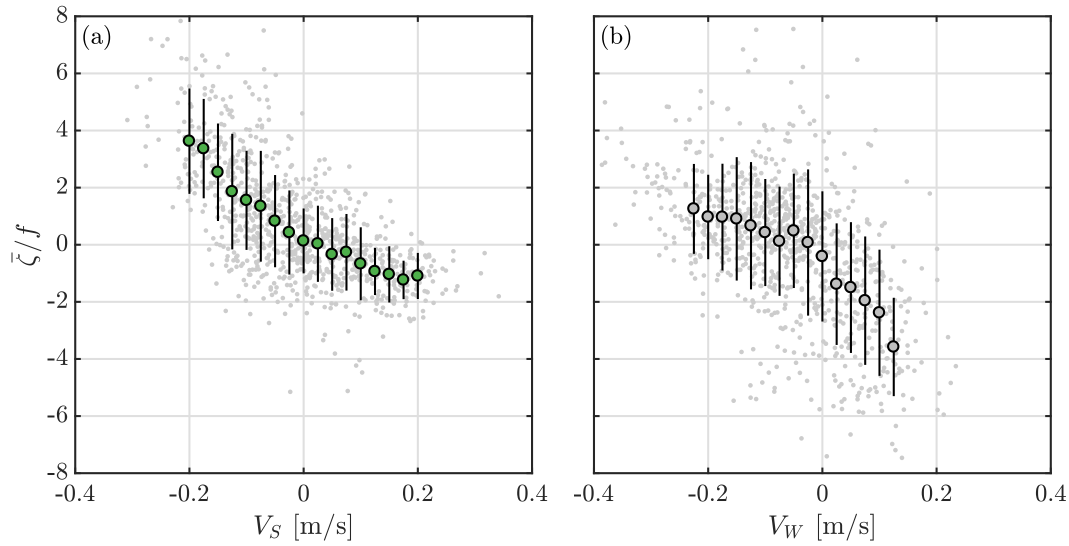

Figure 10. Depth-averaged vorticity versus local depth-averaged principal axis velocity for (a) south location $\bar{\zeta}_{\mathrm{S}}/f$ versus V_{S} and (b) west location $\bar{\zeta}_{\mathrm{W}}/f$ versus V_{W}. Light gray dots are hourly data. Green and gray dots are bin-averaged into 2.5 cm s^{-1} bins, with bin standard deviation indicated by vertical black lines. Bins have a minimum of 15 data points.

scatter in the hourly data (light gray dots and binned-mean std) range from 0.7–2, suggesting other, non-steady processes are also occurring.

At the west location, a similar negative-signed relationship between hourly $\bar{\zeta}_{\mathrm{W}}/f$ and V_{W} is observed, albeit with lower $r^2 = 0.29$ (Figure 10b). The binned-mean $\bar{\zeta}_{\mathrm{W}}/f$ and V_{W} squared correlations ($r^2 = 0.88$) is also tighter. A $\bar{\zeta}_{\mathrm{W}}/f$ and V_{W} slope asymmetry also is evident that depends on the V_{W} sign. However, the west location asymmetry is opposite that of the south location. For both locations at a particular $|V|$, the $|\bar{\zeta}/f|$ is largest when located in the lee of Pt. Sal. This is again consistent with upstream or headland vorticity generation. The $\bar{\zeta}/f$ and V slope in the lee is 1.5× stronger for the west versus the south location (Figure 10), despite the missing $\partial\tilde{u}/\partial\tilde{y}$ in the estimated $\bar{\zeta}_{\mathrm{W}}/f$ (Section 2.2.2). For $V_{\mathrm{W}} > 0$, the $\bar{\zeta}_{\mathrm{W}}/f$ is likely even more negative (Appendix A). The $\bar{\zeta}_{\mathrm{W}}/f$ and V_{W} scatter is larger than at the south location (binned standard deviations are larger and range from 1.5–2.6) without a V_{W} dependence.

The $\bar{\zeta}/f$ (non-dimensional) and V (unit m s^{-1}) relationship (Figure 10) is not dimensionally consistent, and so cannot be generalized to other headlands. However, the $\bar{\zeta}/f$ and V relationship can help understand the length-scales of the headland wake vorticity. For example, $V_{\mathrm{S}} = -0.2$ m s^{-1} on average corresponds to $\bar{\zeta}_{\mathrm{S}}/f = 3.8$. With a vorticity scaling as V/L_{v} this implies a wake vorticity length-scale of $L_{\mathrm{v}} = 630$ m, qualitatively consistent with Figure 1 and the assumed $L \sim 1$ km headland scale. At the west location, binned-mean $\bar{\zeta}_{\mathrm{W}}/f = 3.5$ for $V_{\mathrm{W}} = -0.12$ m s^{-1}, resulting in a somewhat shorter length-scale $L_{\mathrm{v}} = 410$ m. Where Pt. Sal sits in non-dimensional parameter space will be explored in the Discussion.

At the south and west locations, the bin-averaged $\bar{\zeta}/f$ and V relationship (Figure 10) indicates a consistency with steady flow concepts as well as headland or farther upstream vorticity generation. However, the scatter in the relationship suggests that the time-varying (oscillatory) nature of the flow may also play an important role in vorticity evolution.

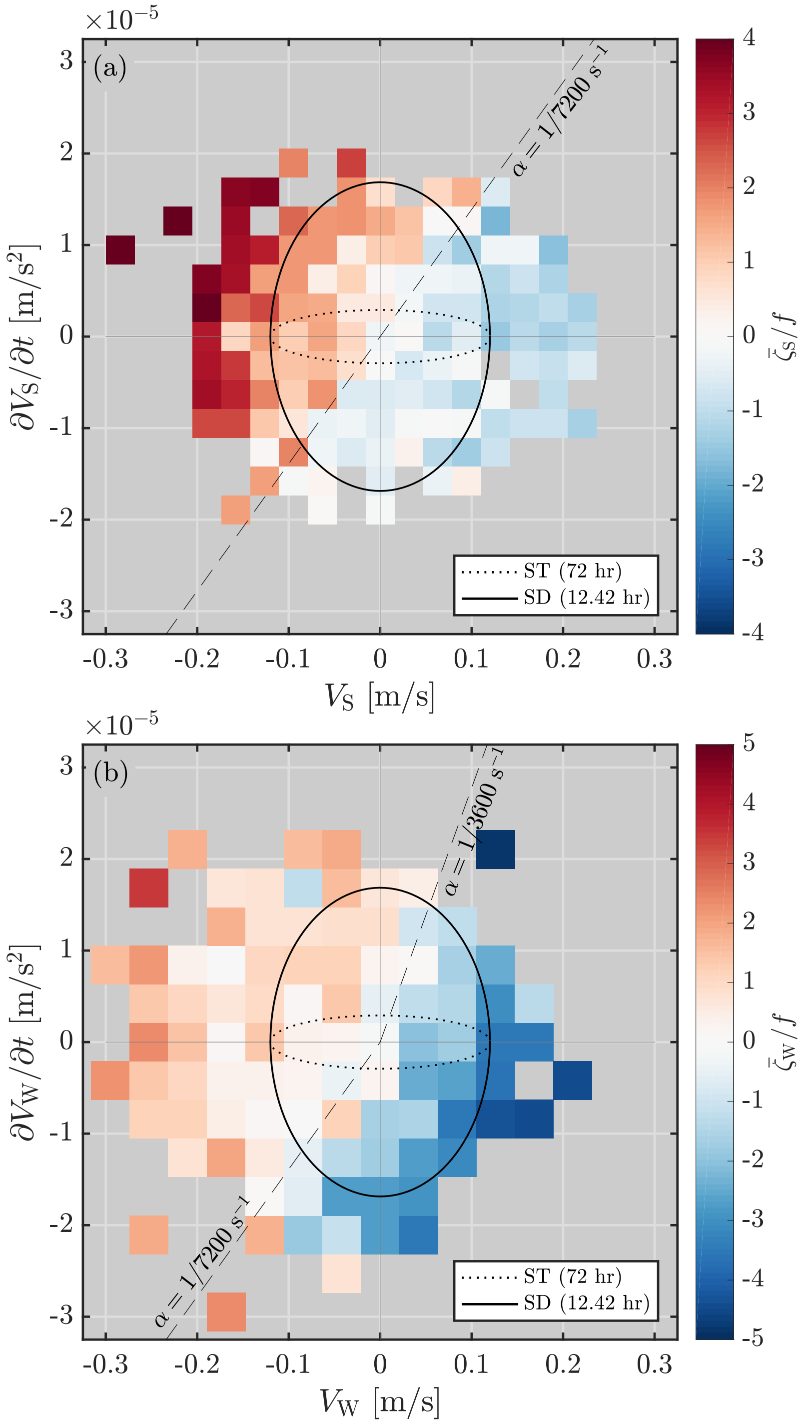

Figure 11. Bin-meaned $\bar{\zeta}/f$ (colored) as a function of the depth-averaged principal axis velocity V and acceleration $\partial V/\partial t$ at (a) south location and (b) west location. Bins with fewer than three data points are removed. In (a) dashed line shows a zero-vorticity slope (6) of $\alpha = 1/7200\ \mathrm{s}^{-1}$ and in (b) the dashed line has $\alpha = 1/3600\ \mathrm{s}^{-1}$ and $\alpha = 1/7200\ \mathrm{s}^{-1}$ in the upper-right and lower-left quadrants, respectively. In (a,b), the solid and dotted ellipses show the clockwise orbital paths in V_S and $\partial V_\mathrm{S}/\partial t$ phase space of a semi-diurnal (SD, 12.42 h period) and subtidal (ST, 72 h period) periodic flow (11) with amplitude of 0.12 $\mathrm{m\,s^{-1}}$.

At both south and west locations, the binned-mean $\bar{\zeta}/f$ depends strongly on both V and local acceleration $\partial V/\partial t$ (Figure 11). Note that time-varying flow moves clockwise in V and $\partial V/\partial t$ phase space in Figure 11 and has to cross $\partial V/\partial t = 0$ for V to have an extrema. Considering first the south location and times of weak acceleration $\partial V_{\mathrm{S}}/\partial t \approx 0$, binned-averaged $\bar{\zeta}_{\mathrm{S}}/f$ is related to $-V_{\mathrm{S}}$, consistent with Figure 10a. In a pure steady flow paradigm, $V_{\mathrm{S}} \approx 0$ should give $\bar{\zeta}_{\mathrm{S}}/f \approx 0$. However, for $V_{\mathrm{S}} \approx 0$, binned-averaged $\bar{\zeta}_{\mathrm{S}}/f$ is largely proportional to $\partial V_{\mathrm{S}}/\partial t$. For example, with $V_{\mathrm{S}} \approx 0$, $\bar{\zeta}_{\mathrm{S}}/f \approx 2$ for positive $\partial V_{\mathrm{S}}/\partial t = 1.5 \times 10^{-5}$ m s^{-2} indicating that the previously generated positive vorticity from earlier southward flow ($V_{\mathrm{S}} < 0$) is still present. Moving through phase space, as V_{S} becomes positive and as $\partial V_{\mathrm{S}}/\partial t > 0$ continues, $\bar{\zeta}_{\mathrm{S}}/f$ remains positive as previously generated positive $\bar{\zeta}_{\mathrm{S}}/f$ is advected back northward (upper right quadrant, Figure 11a), suggesting vorticity is recirculating across the headland. Later, as positive (northward) V_{S} strengthens and $\partial V_{\mathrm{S}}/\partial t$ weakens, bin-average $\bar{\zeta}_{\mathrm{S}}/f$ undergoes a sign transition and becomes negative. This $\bar{\zeta}_{\mathrm{S}}/f$ sign transition (*i.e.*, $\bar{\zeta}_{\mathrm{S}}/f = 0$) occurs on the *zero vorticity slope*

$$\alpha = \frac{\partial V_{\mathrm{S}}/\partial t}{V_{\mathrm{S}}} \tag{6}$$

of $\alpha \approx 1/7200$ s^{-1} (dashed line in Figure 11a) suggesting a vorticity adjustment timescale of ≈ 2 h (Section 6.1). As V_{S} goes from positive to negative and $\partial V_{\mathrm{S}}/\partial t < 0$ (lower left quadrant, Figure 11a), a similar $\bar{\zeta}_{\mathrm{S}}/f$ sign transition occurs, with similar zero vorticity slope α, indicating a symmetric response with V_{S} sign change. South location vorticity recirculation is evident for $|\partial V_{\mathrm{S}}/\partial t| > 0.3\times10^{-5}$ m s^{-2}. These observations demonstrate that previously generated $\bar{\zeta}/f$ can be advected back across the headland before significant vorticity generation can take place. This is consistent with oscillatory wake flow concepts and modeled tidal headland eddies of Signell & Geyer (1991).

At the west location, the relationship of $\bar{\zeta}_{\mathrm{W}}/f$ to V_{W} and $\partial V_{\mathrm{W}}/\partial t$ is qualitatively similar to the south location, with clear time-varying flow effects (Figure 11b). Comparing the south and west location, V_{W} is more often negative than V_{S} and $\bar{\zeta}_{\mathrm{W}}/f$ is more strongly negative whereas $\bar{\zeta}_{\mathrm{S}}/f$ is more strongly positive, consistent with Figures 6 and 10. As noted previously, for $V_{\mathrm{W}} > 0$, the negative $\bar{\zeta}_{\mathrm{W}}/f$ may be biased to low magnitudes (Appendix A). West location vorticity recirculation is not as clear as at the south location but is clearly evident for $\partial V_{\mathrm{W}}/\partial t < -10^{-5}$ m s^{-2}. The zero vorticity slopes (6) are different as V_{W} changes sign with positive $\partial V_{\mathrm{W}}/\partial t$ versus negative $\partial V_{\mathrm{W}}/\partial t$ (compare upper-right to lower-left quadrants, respectively, in Figure 11b). As V_{W} becomes positive with positive $\partial V_{\mathrm{W}}/\partial t$, the zero-vorticity slope is approximately $\alpha \approx 1/3600$ s^{-1} (upper right dashed line in Figure 11b), about twice as steep as for the south location. As V_{W} becomes negative with negative $\partial V_{\mathrm{W}}/\partial t$, the zero-vorticity slope $\alpha \approx 1/7200$ s^{-1} (lower left dashed line in Figure 11b), similar to the south location. This implies an asymmetric $\bar{\zeta}_{\mathrm{W}}/f$ response to V_{W} changing sign, with a much faster transition from southward to northward flow (upper right quadrant, Figure 11b) than from northward to southward flow (lower left quadrant, Figure 11b). This suggests asymmetry of vorticity generation processes with different sign of mean flow at the west location, in particular, that negative vorticity may be rapidly generated as flow switches to northward.

5 Asymmetric Vorticity Generation at the Headland

The local vorticity-velocity relationship (Figure 10) suggests vorticity generation at the headland or farther upstream. Here, headland vorticity generation is inferred from estimates of the potential vorticity change across the headland (west and south locations).

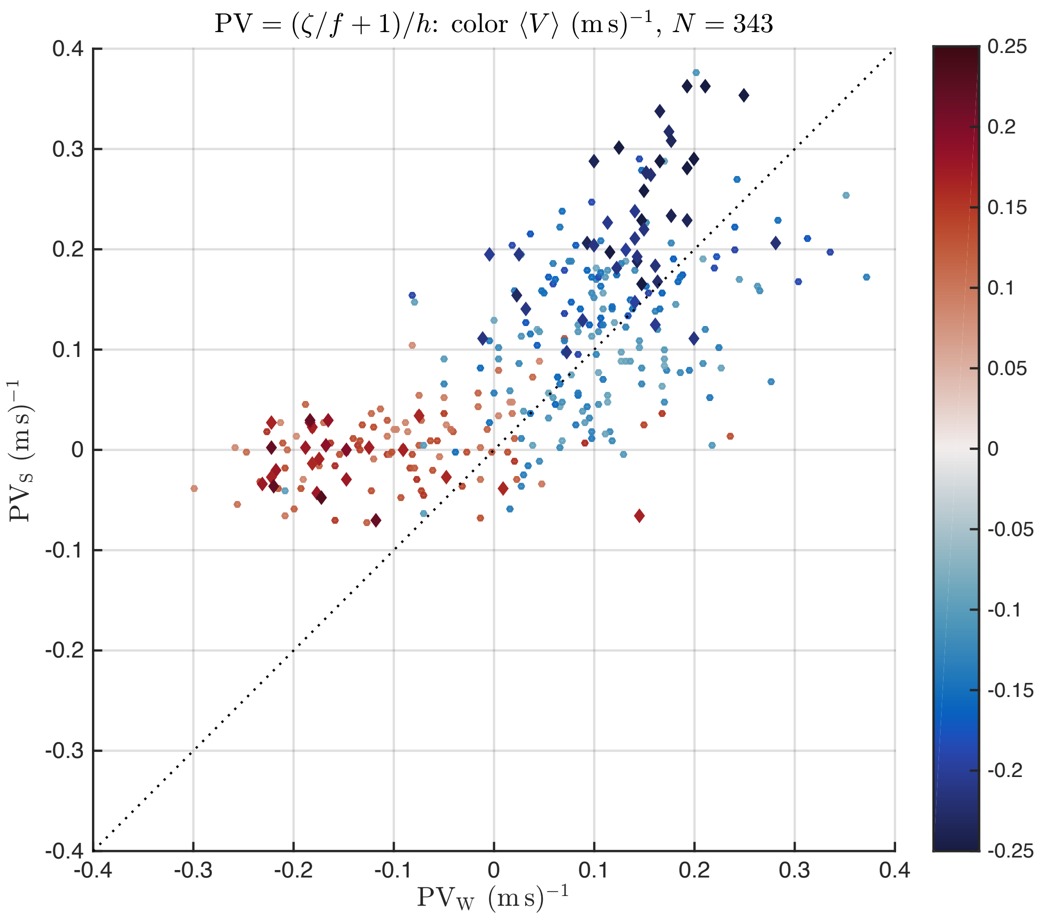

Figure 12. Potential Vorticity (PV) at the south ($\mathrm{PV_S}$) location versus west ($\mathrm{PV_W}$) location with symbols colored by the west and south averaged principal axes velocity $\langle V \rangle$ (10). Observations are limited quasi-steady conditions with $|\langle V \rangle| > 0.08\ \mathrm{m\,s^{-1}}$ and $|\partial \langle V \rangle / \partial t| < 10^{-5}\ \mathrm{m\,s^{-2}}$, yielding 343 out of 928 hourly data points. Blue and red diamonds highlight data points where $\langle V \rangle \leq -0.2\ \mathrm{m\,s^{-1}}$ (43 data points) and $\langle V \rangle \geq 0.16\ \mathrm{m\,s^{-1}}$ (25 data points). Note, four data points lie outside the axes limits.

Potential vorticity PV is defined as

$$\mathrm{PV} = \frac{\bar{\zeta}/f + 1}{h}, \tag{7}$$

and estimated at south and west locations with $h_\mathrm{S} = 22.5$ m and $h_\mathrm{W} = 19.0$ m. In an inviscid and homogeneous shallow water system, PV is conserved,

$$\frac{D(\mathrm{PV})}{Dt} = 0. \tag{8}$$

In a quasi-steady flow (*i.e.*, $\partial_t(\mathrm{PV})$ is small) and assuming that the west and south locations are upon the same streamline with uniform velocity, (8) simplifies to

$$\mathrm{PV_S} = \mathrm{PV_W}. \tag{9}$$

With bottom friction, potential vorticity can be generated, and deviations from (9) between upstream and downstream locations can be interpreted as headland PV generation, under the above assumptions. Here, we address potential vorticity generation at the Pt. Sal headland by comparing $\mathrm{PV_W}$ to $\mathrm{PV_S}$ as a function of south and west location averaged principal axes velocity $\langle V \rangle$ defined as

$$\langle V \rangle = \frac{1}{2}(V_{\mathrm{S}} + V_{\mathrm{W}}). \tag{10}$$

As the analysis of PV generation assumes quasi-steady conditions, we limit observations to times when $|\partial \langle V \rangle / \partial t| < 10^{-5}\ \mathrm{m\,s^{-2}}$ and $|\langle V \rangle| > 0.08\ \mathrm{m\,s^{-1}}$ based on Figure 11. Recall that V_{S} and V_{W} were highly correlated with $r = 0.86$ (Figure 6b). The results below are not dependent on the chosen $\langle V \rangle$ and $\partial \langle V \rangle / \partial t$ cutoffs.

The relationship between $\mathrm{PV_S}$ and $\mathrm{PV_W}$ as a function of $\langle V \rangle$ is shown in Figure 12. For southward flow $\langle V \rangle < -0.08\ \mathrm{m\,s^{-1}}$, both $\mathrm{PV_W}$ and $\mathrm{PV_S}$ are generally both positive and increase with more negative $\langle V \rangle$ (blue colors in Figure 12), although occasionally PV at one or both locations is also negative. When both $\mathrm{PV_S}$ and $\mathrm{PV_W}$ are positive with $\langle V \rangle < -0.08\ \mathrm{m\,s^{-1}}$, no clear trend above or below the 1:1 line is evident and a best-fit to those data yield a slope slightly < 1. However, for the strongest southward flow $\langle V \rangle < -0.2\ \mathrm{m\,s^{-1}}$, nearly all 43 data points have $\mathrm{PV_S} > \mathrm{PV_W}$ by a factor of $1.5\times$ to $2\times$ (diamonds in Figure 12). Under the above assumptions (steady and on a streamline), this suggests that headland vorticity (PV) generation is weak for relatively weak southward flow (and implies vorticity generation upstream of the west location), but significant PV generation occurs for stronger southward flow.

For northward flow $\langle V \rangle > 0.08\ \mathrm{m\,s^{-1}}$ (red colors in Figure 12), PV generation is clearly indicated under the above assumptions. At the upstream (south) location for $\langle V \rangle > 0.08\ \mathrm{m\,s^{-1}}$, $\mathrm{PV_S}$ is generally small within $\pm 0.1\ (\mathrm{m\,s})^{-1}$ with a near-zero mean. Overall, $\mathrm{PV_S} < 0$ is uncommon (see also the uncommon $\bar{\zeta}_{\mathrm{S}}/f < -1$ in Figure 7). Most of the corresponding $\mathrm{PV_W}$ are negative, varying between -0.3 and $0\ (\mathrm{m\,s})^{-1}$ and are substantially more negative than $\mathrm{PV_S}$. For larger $\langle V \rangle > 0.16\ \mathrm{m\,s^{-1}}$ (red diamonds in Figure 12), $\mathrm{PV_W}$ is generally more negative (mean of $-0.14\ (\mathrm{m\,s})^{-1}$) whereas $\mathrm{PV_S} \approx 0$. This suggest that for northward flow, on average, substantial PV is generated at the headland. Note that for northward flow, the negative $\bar{\zeta}_{\mathrm{W}}$ is likely biased to low magnitudes (Appendix A) and that $\bar{\zeta}_{\mathrm{W}}$ and thus $\mathrm{PV_W}$ is likely even more negative. The difference between northward and southward flow suggests asymmetry in headland vorticity generation.

6 Discussion

6.1 Phase space of different flow time-scales

Steady flow concepts indicate strong vorticity generation for northward flow and weak vorticity generation only for stronger southward flow. For realistic time-dependent flows, Pt. Sal vorticity depends upon V and $\partial V/\partial t$ (Figure 11), consistent with pure periodic flow concepts. At Pt. Sal, the depth-averaged principal axes V is composed of semi-diurnal, diurnal, and subtidal (> 33 h) flow time-scales that move through V and $\partial V/\partial t$ phase space. Here, lower and higher frequency flows movement through $(V, \partial V/\partial t)$ phase space (ellipses in Figure 11) in relation to vorticity recirculation and generation is examined using a periodic velocity

$$V(t) = V_0 \cos(\omega t), \tag{11}$$

for semidiurnal (12.42 h period, ω_{sd}) or a subtidal (72 h period, ω_{st}) radian frequencies corresponding to the dominant variability of V (Figure 6b). The subtidal radian frequency corresponding to 72 h is chosen as a representative subtidal frequency. The semidiurnal and subtidal velocity amplitude both are assigned $V_0 \approx 0.12\ \mathrm{m\,s^{-1}}$ corresponding to the semidiurnal spring tide amplitudes and subtidal velocity amplitude (std times $\sqrt{2}$). For periodic flow, the vorticity adjustment time-scale t_α is the time to go from $V = 0$ to crossing the zero-vorticity ($\bar{\zeta}/f = 0$) slope $\alpha = \partial V/\partial t/V$ defined as,

$$t_\alpha = \omega^{-1} \cot^{-1}\left(\frac{\alpha}{\omega}\right), \tag{12}$$

and for $\alpha/\omega \ll 1$, $t_\alpha \to \alpha^{-1}$. The advective recirculation distance L_α over the vorticity adjustment time-scale t_α is approximately,

$$L_\alpha = V_0\omega^{-1}\left[1 - \cos(\omega t_\alpha)\right]. \tag{13}$$

For subtidal (72 h) flow, the phase space ellipse is eccentric with relatively weak accelerations ($< 4 \times 10^{-6}\ \mathrm{m\,s^{-2}}$, Figure 11 dotted ellipse), implying that $\bar{\zeta}/f$ is predominantly a function of V. The subtidal orbital excursion amplitude $V_0/\omega_{\mathrm{st}} \approx 5000$ m, greater than the separation between the west and south locations ($L_{\mathrm{W,S}} \approx 1200$ m). At subtidal periods, the $\bar{\zeta}/f = 0$ slope for $\alpha = (1/7200)\ \mathrm{s^{-1}}$ is crossed in $t_\alpha = 2$ h, allowing only $L_\alpha \approx 75$ m of recirculated vorticity prior to the V sign switch, substantially less than $L_{\mathrm{W,S}} \approx 1200$ m. For $\alpha = (1/3600)\ \mathrm{s^{-1}}$ the vorticity adjustment time-scale $t_\alpha \approx 1$ h, and the recirculation distance $L_\alpha = 19$ m is even shorter. Subtidal velocity variability is often red, and using subtidal periods longer than 72 h in (12) and (13) results in even shorter recirculation distances.

For semidiurnal oscillatory flow, the accelerations are much stronger, up to $1.7 \times 10^{-5}\ \mathrm{m\,s^{-2}}$, resulting in $\bar{\zeta}/f$ that depends on both V and $\partial V/\partial t$ (Figure 11, solid ellipse). The semidiurnal orbital excursion amplitude $V_0/\omega_{\mathrm{sd}} \approx 850$ m is less than $L_{\mathrm{W,S}} \approx 1200$ m. For $\alpha = (1/7200)\ \mathrm{s^{-1}}$, the semidiurnal vorticity adjustment time-scale $t_\alpha = 1.5$ h, with $L_\alpha = 250$ m of recirculation. For semidiurnal flow and $\alpha = (1/3600)\ \mathrm{s^{-1}}$, the recirculation distance is even smaller $t_\alpha = 1$ h and $L_\alpha = 92$ m.

The recirculation distances for subtidal ($L_\alpha = 75$ m) and semidiurnal ($L_\alpha = 250$ m) are small relative to the ≈ 1200 separation between W and S centroid locations. In a time-varying paradigm, vorticity switching sign before a water parcel could advect a distance $L_{\mathrm{W,S}}$ (Figure 11) suggests consistent headland vorticity generation for both northward and southward flow even at semidiurnal time-scales. This is consistent with the steady-flow paradigm of inferred PV generation for northward flow (red in Figure 12) and for stronger southward flow (blue diamonds). However, for southward flow, the steady-flow paradigm only suggested PV generation for strong southward flow (blue diamonds in Figure 12). This difference may reflect a limitation of the assumptions of steady flow on a streamline in the potential vorticity analysis (Section 5). Flow variability at Pt. Sal is dominated by semidiurnal and lower frequency variability. Although the actual $(V, \partial V/\partial t)$ phase space path involves a range of time-scales, all semidiurnal and longer time-scales will give $L_\alpha < L_{\mathrm{W,S}}$. As a vorticity adjustment time-scale is evident at the south location for $|\partial V_{\mathrm{S}}/\partial t| > 0.3 \times 10^{-5}\ \mathrm{m\,s^{-2}}$, these conclusions apply to any time-scale present in the flow with sufficient acceleration magnitude.

6.2 Dimensional and non-dimensional parameter space

Here, we contextualize Pt. Sal relative to other observed headland and island wakes in both dimensional and non-dimensional parameter space. Pt. Sal has characteristic length-scale $L \sim 1$ km (Figure 1) consistent with TTP (*e.g.,* MacCready & Pawlak, 2001) and the Zandmotor (Radermacher et al., 2017), but considerably smaller than Velasco Reef, Palau $L \sim 10$ km (MacKinnon et al., 2019). Note, the Zandmotor is a low sloped (low aspect ratio) feature, in contrast to the sharp (high aspect ratio) features of Pt. Sal, TTP, and Velasco Reef. The Pt. Sal characteristic depth $h \sim 20$ m is similar to the Zandmotor ($h \sim 10$ m), but much shallower than the 200 m and 600 m depths of TTP and Velasco Reef (MacCready & Pawlak, 2001; MacKinnon et al., 2019). The Coriolis parameter $f = 8.3 \times 10^{-5}$ s^{-1} is characteristic of mid-latitudes, but is four times larger than that for the near-equatorial Palau ($f = 2.1 \times 10^{-5}$ s^{-1}). The Pt. Sal principal axes currents are broadband (Figure 6b) similar to Velasco Reef (MacKinnon et al., 2019) contrasting with the primarily tidal flow of TTP and Zandmotor. Based on the variance in each of the semidiurnal and subtidal bands, the velocity scale is $U \sim 0.12$ m s^{-1} for each and a total of $U \sim 0.2$ m s^{-1}. This is similar to TTP ($U_0 \sim 0.2$ m s^{-1}), weaker than the semidiurnal tidal velocity at Velasco Reef ($U_0 \sim 0.4$ m s^{-1}), and substantially weaker than the Zandmotor ($U_0 \sim 0.7$ m s^{-1}). The sea-bed near Pt. Sal is generally composed of medium grain sand, and a bulk quadratic drag coefficient $C_D = 2{\times}10^{-3}$ is used for depth-averaged flow. This embeds the surface gravity wave enhanced bottom stress within C_D (Feddersen et al., 2000; Lentz et al., 2018). Note that near Pt. Sal, the bed is rocky reef with large roughness. The semidiurnal (12.42 h) radian frequency $\omega_{\mathrm{sd}} \approx 1.4 \times 10^{-4}$ s^{-1}. The subtidal time-scale is broadband but here as above we ascribe a 72 h subtidal radian frequency $\omega_{\mathrm{st}} = 2.4 \times 10^{-5}$ s^{-1}.

In terms of non-dimensional parameters, we estimate the Pt. Sal Rossby number ($\mathrm{Ro} = U/fL$) with the full $U \sim 0.2$ m s^{-1} resulting in $\mathrm{Ro} \sim 2.4$, a value near Velasco Reef and TTP ($\mathrm{Ro} \sim 0.9$, $\mathrm{Ro} \sim 2$, respectively MacKinnon et al., 2019; Canals et al., 2009), and smaller than Zandmotor $\mathrm{Ro} \sim 6.1$ (Radermacher et al., 2017). Note, the Velasco Reef near-one Ro is due to both the much larger L and a smaller f than Pt. Sal. The Pt. Sal frictional Reynolds number ($\mathrm{Re_f} = h/C_D L$) is estimated as $\mathrm{Re_f} \sim 10$, which, as TTP and Velasco reef are in deep water, can only be compared to Zandmotor at $\mathrm{Re_f} \sim 5$. As the flow has multiple time-scales (*i.e.,* broadband), estimating the ratio of flow excursion to headland length scale $K_c = U_0/(\omega L)$ is challenging. Here we use the spring-tide $U_0 = 0.12$ m s^{-1} and ω_{sd} to estimate a semi-diurnal $K_c^{(\mathrm{sd})} \sim 0.85$, indicating that that vorticity can be weakly recirculated over a tidal cycle. The Pt. Sal $K_c^{(\mathrm{sd})}$ is substantially smaller than the $K_c^{(\mathrm{sd})} \sim 5.0$ of the Zandmotor, but similar to $K_c^{(\mathrm{sd})} = 1.4$ of TTP, and substantially larger than the $K_c^{(\mathrm{sd})} = 0.14$ of Velasco Reef. The Pt. Sal $K_c^{(\mathrm{sd})}$ results in $\mathrm{Re_f}/K_c^{(\mathrm{sd})} \sim 12$ suggesting that the vorticity decay time-scale is longer than a semidiurnal period. As the vorticity adjustment time-scale $t_\alpha < 2$ h (Section 6.1, Figure 11), this further suggests that vorticity generation at the headland is dominant. In contrast, the Zandmotor $\mathrm{Re_f}/K_c^{(\mathrm{sd})} \sim 1$ consistent with the headland eddy decaying within a tidal time-scale (Radermacher et al., 2017).

Here, we have examined depth-averaged vorticity and flow at Pt. Sal and neglected stratification effects. In other headland vorticity generation regions, stratification is important. The Pt. Sal time-average buoyancy frequency $N \sim 0.016$ s^{-1}, estimated from the mean top-to-bottom temperature differences at the thermistor moorings near Pt. Sal, and the local deformation radius $L_d \sim 3.8$ km leads to a Burger number of $L_d/L \sim 3.8$. The buoyancy frequency (stratification) at TTP ($N \sim 0.01$ s^{-1}) and Velasco Reef ($N \sim 0.02$ s^{-1}) are similar, leading to much larger Burger number at TTP $L_d/L = 18$ and Velasco Reef $L_d/L = 50$. Thus, the vorticity generated at Pt. Sal will adjust to geostrophy more rapidly than at TTP and Velasco Reef. Note, no stratification was reported for the ZandMotor. At both TTP and Velasco Reef, the Froude number regime allows for both internal lee waves as well as vorticity generation (Warner & MacCready, 2014; Voet et al., 2020). For flow traveling past Pt. Sal, no coherent obstacle is present (Figure 3), that would allow for lee wave generation even with the strong stratification.

7 Summary

As part of the Inner Shelf Dynamics Experiment (Kumar et al., 2020), two months of fixed ADCP velocity measurements in ~ 20 m depth near the asymmetric headland Pt. Sal CA are used to investigate headland vorticity generation and recirculation. Pt. Sal is a sharp (120° bend) rocky headland with scale of ~ 1 km. To reduce vorticity estimation noise, ADCP velocities were low-pass filtered with a 2 h time-scale and were reconstructed from the first two EOF modes that represented $\approx 73\%$ of the variance. Depth-averaged vorticity was estimated at two locations west and south of Pt. Sal from the smoothed reconstructed velocities of groups of fixed ADCPs. Only one west-location vorticity component was estimated, leading to negative vorticity bias for northward flow. Vorticity was also estimated from multiple parallel vessel transects on a single day. The observed depth-averaged flow principal axes velocity V was primarily along-bathymetric contours and varied largely between ± 0.2 m s^{-1} across subtidal, diurnal, and semidiurnal frequency bands. At west and south locations, the V was well correlated at $r = 0.86$. The south location vorticity is consistent with vorticity estimated from parallel vessel transects on a single day. The vorticity variability was vertically coherent and primarily depth-uniform.

Vertical vorticity kinematics and dynamics were studied with the depth averaged vorticity $\bar{\zeta}/f$. At west and south locations, the depth-averaged normalized vorticity $\bar{\zeta}/f$ varied ± 8 across subtidal, diurnal, semidiurnal, and supertidal frequency bands, had more high frequency variability than V, and was less correlated ($r = 0.55$) than for V. The vorticity distributions are skewed with opposite sign at west and south locations. Negative PV ($\bar{\zeta}/f < -1$) is more likely at both locations than open ocean suggesting strong vorticity generation. At west and south locations, $\bar{\zeta}/f$ and V were related, but asymmetrically with sign of V, indicating vorticity generation at the headland or farther upstream. Analysis within both steady flow and time-varying flow paradigms indicates asymmetric vorticity generation across the headland. Binned-mean $\bar{\zeta}/f$ depends on both V and $\partial V/\partial t$, and indicates vorticity recirculation across the headland as V switches sign. The time-scale for vorticity adjustment is ~ 2 h, and the associated short excursion distances indicate generation between south and west locations, with stronger generation at west location for the transition to northward flow. For quasi-steady flow, the south and west potential vorticity relationship indicates asymmetric vorticity generation between the south and west locations, with stronger vorticity generation for northward flow. The inferred asymmetric vorticity generation for northward flow is consistent with $\bar{\zeta}/f < -1$ more likely at the west location than south location. Pt. Sal occupies a portion of non-dimensional parameter space that is unique relative to other well studied headlands.

Appendix A Vorticity estimation bias at west location

As $\bar{\zeta}_{\mathrm{W}}$ was estimated from two ADCPs, only one component of vertical vorticity $\partial\tilde{v}/\partial\tilde{x}$ was calculated and $\partial\tilde{u}/\partial\tilde{y}$ was neglected, where $(\tilde{y}, \tilde{v})$ represents the principal axes direction and flow magnitude, respectively (Section 2.2.2). In Sections 4 and 5, $\bar{\zeta}_{\mathrm{W}}$ is analyzed in the context of headland generation or unsteady-flow induced recirculation. However, these results could instead be due to noise and bias in the $\bar{\zeta}_{\mathrm{W}}$ estimation method. Here, potential biases in west location vorticity estimates are qualitatively examined using characteristic examples southward and northward flow (Figure A1) and implications for results are discussed.

First consider southward flow from 13-Sept-2017 12:00PDT (Figure A1a), one hour after the vessel survey concluded (Figure 9). South ADCP (green squares) depth-averaged velocities bend (or rotate) south to south east while velocity decreases from 9 cm s^{-1} to

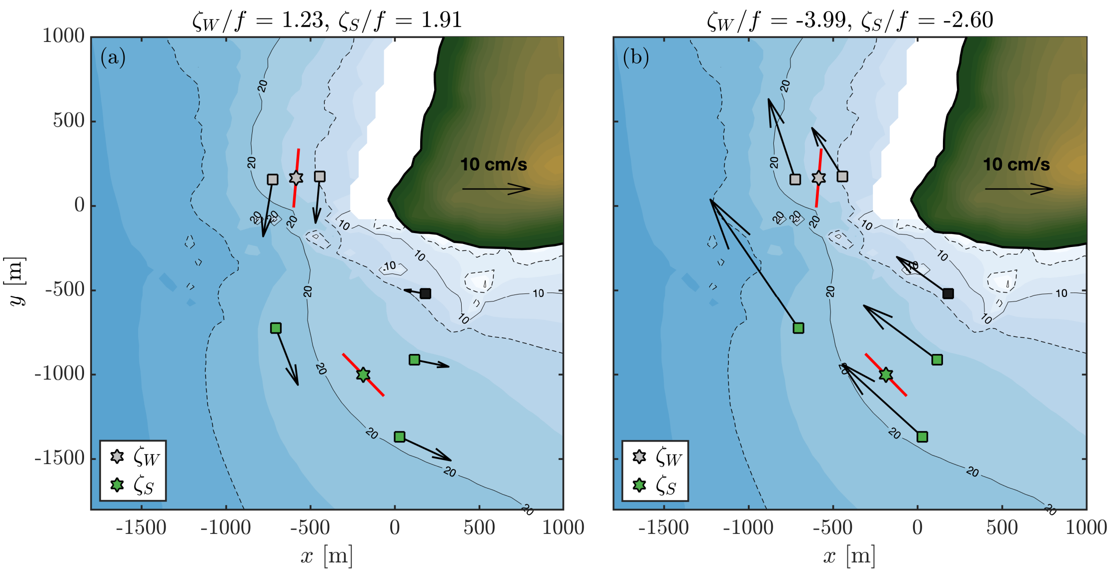

Figure A1. Depth-averaged velocity examples near Pt. Sal to illustrate west location vorticity bias: (a) Southward flow on 13-Sept-2017 12:00 PDT with $\bar{\zeta}_\mathrm{W}/f = 1.23$ and $\bar{\zeta}_\mathrm{S}/f = 1.91$ and (b) Northward flow on 28-Sept-2017 12:00 PDT with $\bar{\zeta}_\mathrm{W}/f = -3.99$ and $\bar{\zeta}_\mathrm{S}/f = -2.60$. Squares represent ADCP locations and black arrows represent depth-averaged velocities. Stars are vorticity estimation locations and the red line gives the orientation of the fit-velocity principal axes. Gray and green markers represent west and south ADCPs and vorticity estimation locations, respectively (see also Figure 3). The solid and dashed lines represent the 15, 20, and 25 m depth contours.

5 $\mathrm{cm\,s^{-1}}$ with decreasing depth, giving a sense of positive vorticity. Both components of vorticity ($\partial\tilde{v}/\partial\tilde{x}$ and $\partial\tilde{u}/\partial\tilde{y}$) are important to the estimated $\bar{\zeta}_\mathrm{S}/f = 1.91$. The west ADCPs (gray squares in Figure A1a) have a southward, roughly along-isobath, 7–9 $\mathrm{cm\,s^{-1}}$ depth-averaged flow in the principal axes direction with larger magnitude at the offshore location, suggesting positive vorticity. The west estimated $\bar{\zeta}_\mathrm{W}/f = 1.23$ using only $\partial\tilde{v}/\partial\tilde{x}$ (Section 2.2.2). At this time, the west velocities perpendicular to the principal axes direction are weak with ADCP averaged $\tilde{u} = 0.4\ \mathrm{cm\,s^{-1}}$, much smaller than characteristic $\tilde{v}$. An ADCP farther upstream (north) in the principal axes direction would likely have near-zero depth-averaged onshore flow (*i.e.,* $\tilde{u} \approx 0$) due to the coastline boundary. This would on average lead to $|\partial\tilde{u}/\partial\tilde{y}| \ll |\partial\tilde{v}/\partial\tilde{x}|$ for southward flow. Thus, $\bar{\zeta}_\mathrm{W}$ may have unbiased error that the statistical analysis of Sections 4 and 5 reduces, we argue that the bias is weak for southward flow.

The northward flow example (Figure A1b) suggests potential northward flow bias in the west location vorticity due to west location cross-principal axis flow. At the south ADCP (green squares), the flow is to the NW at 13–23 $\mathrm{cm\,s^{-1}}$ in the principal axes direction (red line at green star). The depth-averaged flow variation parallel and perpendicular to the principal axes direction both suggest negative vorticity, and the estimated $\bar{\zeta}_\mathrm{S}/f = -2.60$ using both components of vorticity. At the west location (gray squares in Figure A1b), the depth-averaged flow is also NW at 9–13 $\mathrm{cm\,s^{-1}}$ with faster flow offshore. However, the depth-averaged velocities are not aligned with the principal axis direction (red line at gray star), with the ratio of cross-axis to along-axis velocity $\tilde{u}/\tilde{v}$ ratio of 0.75 and 0.43 at shallow and deeper west ADCP locations, respectively. The $\partial\tilde{v}/\partial\tilde{x}$ estimated $\bar{\zeta}_{\mathrm{W}}/f = -3.99$ is larger than the $\bar{\zeta}_{\mathrm{S}}/f$ estimate, suggesting vorticity generation, but is likely biased by not including $\partial\tilde{u}/\partial\tilde{y}$. To constrain the sign of the bias, consider an ADCP farther to the north in the lee of Pt. Sal along the principal axis direction. This ADCP would likely have $\tilde{u} \approx 0$ as depth-averaged onshore flow is limited by the boundary (as for southward flow) and $\partial\tilde{u}/\partial\tilde{y}$ would be positive. Thus, the true vorticity $\bar{\zeta}_{\mathrm{W}} = \partial\tilde{v}/\partial\tilde{x} - \partial\tilde{u}/\partial\tilde{y}$ would be even more negative. In this case, if west ADCP $\tilde{u}/\tilde{v} = 0.5$ and $\partial\tilde{y} = \partial\tilde{x} = 280$ m, then $\bar{\zeta}_{\mathrm{W}}/f \approx -6$. For northward flow, we qualitatively argue that the $\bar{\zeta}_{\mathrm{W}}$ estimate is positively biased, and that the true west vorticity is even more negative than estimated. Thus, the inference of strong potential vorticity generation for northward flow (Section 5) is likely accurate but the generation rate is underestimated.

Acknowledgments

This work was sponsored by the U.S. Office of Naval Research (ONR) in an ONR Departmental Research Initiative (DRI), Inner-Shelf Dynamics Experiment (ISDE). We thank Dr. Reginald Beach for supporting all the initiatives undertaken as a part of this project. We thank Colonel Moss, Commander, 30 SW/CC (2017), Jennifer Tribble, and the operations staff at VAFB for coordinating aircraft access and assisting in recovery of instruments. Jim Thomson drove the RV Sounder transects and graciously provided us with the data. Thank you. We thank Bill Boyd, Greg Boyd, Rob Grenzeback, Lucian Parry, Brett Pickering, Greg Sinnett, Kent Smith, Brian Woodward who assisted with the nearshore Point Sal fieldwork. We thank Luc Lenain, Nick Statom, and W. K. Melville for providing the LWIR image in Figure 1. Sutara (Ata) Suanda, Matt Spydell, Amy Waterhouse, André Palóczy, Sean Celona, and Jen MacKinnon provided valuable feedback on this work. We also thank the two anonymous reviewers whose comments significantly improved the manuscript. Data from the ISDE is being archived at the UC San Diego Library Digital Collects and a DOI will be available upon revision. Data discussed here can be immediately accessed by emailing Dr. Falk Feddersen.

References

Aristizábal, M. F., Fewings, M. R., & Washburn, L. (2017). Effects of the relaxation of upwelling-favorable winds on the diurnal and semidiurnal water temperature fluctuations in the santa barbara channel, california. *Journal of Geophysical Research: Oceans*, *122*(10), 7958-7977. doi: 10.1002/2017JC013199

Canals, M., Pawlak, G., & MacCready, P. (2009). Tilted baroclinic tidal vortices. *Journal of Physical Oceanography*, *39*(2), 333-350. doi: 10.1175/2008JPO3954.1

Castelao, R. M., & Barth, J. A. (2006). The relative importance of wind strength and along-shelf bathymetric variations on the separation of a coastal upwelling jet. *Journal of Physical Oceanography*, *36*(3), 412-425. doi: 10.1175/JPO2867.1

Colosi, J. A., Kumar, N., Suanda, S. H., Freismuth, T. M., & MacMahan, J. H. (2018). Statistics of internal tide bores and internal solitary waves observed on the inner continental shelf off point sal, california. *Journal of Physical Oceanography*, *48*(1), 123-143. doi: 10.1175/JPO-D-17-0045.1

Dong, C., & McWilliams, J. C. (2007). A numerical study of island wakes in the southern california bight. *Continental Shelf Research*, *27*(9), 1233 - 1248. (Recent Developments in Physical Oceanographic Modelling: Part IV) doi: https://doi.org/10.1016/j.csr.2007.01.016

Dong, C., McWilliams, J. C., & Shchepetkin, A. F. (2007). Island wakes in deep water. *Journal of Physical Oceanography*, *37*(4), 962-981. doi: 10.1175/JPO3047.1

Edwards, K., Maccready, P., Moum, J., Pawlak, G., Klymak, J., & Perlin, A. (2004, 06). Form drag and mixing due to tidal flow past a sharp point. *Journal of Physical Oceanography*, *34*, 1297-1312. doi: 10.1175/1520-0485(2004)034⟨1297:FDAMDT⟩2.0.CO;2

Emery, W. J., & Thomson, R. E. (2001). *Data analysis methods in physical oceanography* (2nd ed.). Amsterdam: Elsevier Science.

Farmer, D., Pawlowicz, R., & Jiang, R. (2002). Tilting separation flows: a mechanism for intense vertical mixing in the coastal ocean. *Dynamics of Atmospheres and Oceans*, *36*(1), 43 - 58. (Ocean Fronts) doi: https://doi.org/10.1016/S0377-0265(02)00024-6

Feddersen, F., Guza, R. T., Elgar, S., & Herbers, T. H. C. (2000). Velocity moments in alongshore bottom stress parameterizations. *Journal of Geophysical Research: Oceans*, *105*(C4), 8673-8686. doi: 10.1029/2000JC900022

Feddersen, F., MacMahan, J. H., Freismuth, T. M., Gough, M. K., & Kovatch, M. (2020). Inner-shelf vertical and alongshore temperature variability in the subtidal, diurnal, and semidiurnal bands along the central california coastline with headlands. *Journal of Geophysical Research: Oceans*, *125*(3), e2019JC015347. doi: 10.1029/2019JC015347

Gan, J., & Allen, J. S. (2002). A modeling study of shelf circulation off northern california in the region of the coastal ocean dynamics experiment: Response to relaxation of upwelling winds. *Journal of Geophysical Research: Oceans*, *107*(C9), 6-1-6-31. doi: 10.1029/2000JC000768

George, D., Largier, J., Storlazzi, C., & Barnard, P. (2015). Classification of rocky headlands in california with relevance to littoral cell boundary delineation. *Marine Geology*, *369*, 137 - 152. doi: https://doi.org/10.1016/j.margeo.2015.08.010

Geyer, W. R., & Signell, R. (1990). Measurements of tidal flow around a headland with a shipboard acoustic doppler current profiler. *Journal of Geophysical Research: Oceans*, *95*(C3), 3189-3197. doi: 10.1029/JC095iC03p03189

Hoskins, B. J. (1974). The role of potential vorticity in symmetric stability and instability. *Quarterly Journal of the Royal Meteorological Society*, *100*(425), 480-482. doi: 10.1002/qj.49710042520

Johnston, T. S., MacKinnon, J. A., Colin, P. L., Jr., P. J. H., Lermusiaux, P. F., Lucas, A. J., ... Waterhouse, A. F. (2019, December). Energy and momentum lost to wake eddies and lee waves generated by the north equatorial current and tidal flows at peleliu, palau. *Oceanography*. Retrieved from `https://doi.org/10.5670/oceanog.2019.417`

Kirincich, A. (2016, 08). The Occurrence, Drivers, and Implications of Submesoscale Eddies on the Martha's Vineyard Inner Shelf. *Journal of Physical Oceanography*, *46*(9), 2645-2662. doi: 10.1175/JPO-D-15-0191.1

Kumar, N., Feddersen, F., Uchiyama, Y., McWilliams, J., & OReilly, W. (2015). Midshelf to surfzone coupled roms–swan model data comparison of waves, currents, and temperature: Diagnosis of subtidal forcings and response. *Journal of Physical Oceanography*, *45*(6), 1464-1490. doi: 10.1175/JPO-D-14-0151.1

Kumar, N., et al. (2020). The inner-shelf dynamics experiment. *Bulletin of the American Meteorologial Society*. (submitted)

Kumar, N., Suanda, S. H., Colosi, J. A., Haas, K., Di Lorenzo, E., Miller, A. J., & Edwards, C. A. (2019). Coastal semidiurnal internal tidal incoherence in the santa maria basin, california: Observations and model simulations. *Journal of Geophysical Research: Oceans*, *124*(7), 5158-5179. doi: 10.1029/2018JC014891

Kundu, P. K., & Allen, J. (1976). Some three-dimensional characteristics of low-frequency current fluctuations near the Oregon coast. *Journal of Physical Oceanography*, *6*(2), 181–199. doi: 10.1175/1520-0485(1976)006,0181:STDCOL.2.0.CO;2.

Lentz, S. J., Churchill, J. H., & Davis, K. A. (2018, 07). Coral Reef Drag Coefficients—Surface Gravity Wave Enhancement. *Journal of Physical Oceanography*, *48*(7), 1555-1566. doi: 10.1175/JPO-D-17-0231.1

Lerczak, J., Barth, J. A., & Chickadel, C. (2019). Untangling a web of interactions where surf meets coastal ocean. *Eos*. doi: https://doi.org/10.1029/

2019EO122141

Limeburner, R., Lrish, J. D., Brown, W. S., Halliwell, G. R., Allen, J. S., Winant, C. D., ... others (1985). *Code-2: Moored array and large-scale data report.* Woods Hole Oceanographic Institution.

Lloyd, P. M., Stansby, P. K., & Chen, D. (2001). Wake formation around islands in oscillatory laminar shallow-water flows. part 1. experimental investigation. *Journal of Fluid Mechanics*, *429*, 217–238. doi: 10.1017/S0022112000002822

Lumley, J. L., & Terray, E. A. (1983a). Kinematics of turbulence convected by a random wave field. *Journal of Physical Oceanography*, *13*(11), 2000-2007. doi: 10.1175/1520-0485(1983)013⟨2000:KOTCBA⟩2.0.CO;2

Lumley, J. L., & Terray, E. A. (1983b). Kinematics of turbulence convected by a random wave field. *Journal of Physical Oceanography*, *13*(11), 2000–2007.

MacCready, P., & Pawlak, G. (2001, 01). Stratified flow along a corrugated slope: Separation drag and wave drag. *J. Phys. Oceanogr.*, *31*, 2824-2839.

MacKinnon, J. A., Alford, M. H., Voet, G., Zeiden, K. L., Shaun Johnston, T. M., Siegelman, M., ... Merrifield, M. (2019). Eddy wake generation from broadband currents near palau. *Journal of Geophysical Research: Oceans*, *124*(7), 4891-4903. doi: 10.1029/2019JC014945

McCabe, R. M., MacCready, P., & Pawlak, G. (2006). Form drag due to flow separation at a headland. *Journal of Physical Oceanography*, *36*(11), 2136-2152. doi: 10.1175/JPO2966.1

McSweeney, J. M., Lerczak, J. A., Barth, J. A., Becherer, J., Colosi, J. A., MacKinnon, J. A., ... Waterhouse, A. F. (2020). Observations of shoaling nonlinear internal bores across the central california inner shelf. *Journal of Physical Oceanography*, *50*(1), 111-132. doi: 10.1175/JPO-D-19-0125.1

Melton, C., Washburn, L., & Gotschalk, C. (2009). Wind relaxations and poleward flow events in a coastal upwelling system on the central california coast. *Journal of Geophysical Research: Oceans*, *114*(C11). doi: 10.1029/2009JC005397

Melville, W. K., Lenain, L., Cayan, D. R., Kahru, M., Kleissl, J. P., Linden, P. F., & Statom, N. M. (2016). The modular aerial sensing system. *Journal of Atmospheric and Oceanic Technology*, *33*(6), 1169-1184. doi: 10.1175/JTECH-D-15-0067.1

Merrifield, S. T., Colin, P. L., Cook, T., Garcia-Moreno, C., MacKinnon, J. A., Otero, M., ... Terrill, E. J. (2019, December). Island wakes observed from high-frequency current mapping radar. *Oceanography*. Retrieved from `https://doi.org/10.5670/oceanog.2019.415`

Molinari, R., & Kirwan, A. D. (1975). Calculations of differential kinematic properties from lagrangian observations in the western caribbean sea. *Journal of Physical Oceanography*, *5*(3), 483-491. doi: 10.1175/1520-0485(1975)005⟨0483:CODKPF⟩2.0.CO;2

Ohlmann, J. C., Molemaker, M. J., Baschek, B., Holt, B., Marmorino, G., & Smith, G. (2017). Drifter observations of submesoscale flow kinematics in the coastal ocean. *Geophysical Research Letters*, *44*(1), 330-337. doi: 10.1002/2016GL071537

Pawlak, G., MacCready, P., Edwards, K. A., & McCabe, R. (2003). Observations on the evolution of tidal vorticity at a stratified deep water headland. *Geophysical Research Letters*, *30*(24). doi: 10.1029/2003GL018092

Radermacher, M., de Schipper, M. A., Swinkels, C., MacMahan, J. H., & Reniers, A. J. (2017). Tidal flow separation at protruding beach nourishments. *Journal of Geophysical Research: Oceans*, *122*(1), 63-79. doi: 10.1002/2016JC011942

Roughan, M., Mace, A. J., Largier, J. L., Morgan, S. G., Fisher, J. L., & Carter, M. L. (2005). Subsurface recirculation and larval retention in the lee of a small headland: A variation on the upwelling shadow theme. *Journal of Geophysical Research: Oceans*, *110*(C10). doi: 10.1029/2005JC002898

Rudnick, D. L. (2001). On the skewness of vorticity in the upper ocean. *Geophysical Research Letters*, *28*(10), 2045-2048. doi: 10.1029/2000GL012265

Rudnick, D. L., Zeiden, K. L., Ou, C. Y., Johnston, T. S., MacKinnon, J. A., Alford, M. H., & Voet, G. (2019, December). Understanding vorticity caused by flow passing an island. *Oceanography*. Retrieved from `https://doi.org/10.5670/oceanog.2019.412`

Shcherbina, A. Y., D'Asaro, E. A., Lee, C. M., Klymak, J. M., Molemaker, M. J., & McWilliams, J. C. (2013a). Statistics of vertical vorticity, divergence, and strain in a developed submesoscale turbulence field. *Geophysical Research Letters*, *40*(17), 4706-4711. doi: 10.1002/grl.50919

Shcherbina, A. Y., D'Asaro, E. A., Lee, C. M., Klymak, J. M., Molemaker, M. J., & McWilliams, J. C. (2013b). Statistics of vertical vorticity, divergence, and strain in a developed submesoscale turbulence field. *Geophysical Research Letters*, *40*(17), 4706-4711. doi: 10.1002/grl.50919

Signell, R. P., & Geyer, W. R. (1991). Transient eddy formation around headlands. *Journal of Geophysical Research: Oceans*, *96*(C2), 2561-2575. doi: 10.1029/90JC02029

Spydell, M. S., Feddersen, F., & Macmahan, J. (2019). The effect of drifter gps errors on estimates of submesoscale vorticity. *Journal of Atmospheric and Oceanic Technology*, *36*(11), 2101-2119. doi: 10.1175/JTECH-D-19-0108.1

Stive, M. J., de Schipper, M. A., Luijendijk, A. P., Aarninkhof, S. G., van Gelder-Maas, C., van Thiel de Vries, J. S., … Ranasinghe, R. (2013). A New Alternative to Saving Our Beaches from Sea-Level Rise: The Sand Engine. *Journal of Coastal Research*, *29*(5), 1001 – 1008. doi: 10.2112/JCOASTRES-D-13-00070.1

Suanda, S. H., Kumar, N., Miller, A. J., Di Lorenzo, E., Haas, K., Cai, D., … Feddersen, F. (2016). Wind relaxation and a coastal buoyant plume north of pt. conception, ca: Observations, simulations, and scalings. *Journal of Geophysical Research: Oceans*, *121*(10), 7455-7475. doi: 10.1002/2016JC011919

Voet, G., Alford, M. H., MacKinnon, J. A., & Nash, J. D. (2020, 05). Topographic Form Drag on Tides and Low-Frequency Flow: Observations of Nonlinear Lee Waves over a Tall Submarine Ridge near Palau. *Journal of Physical Oceanography*, *50*(5), 1489-1507. doi: 10.1175/JPO-D-19-0257.1

Warner, S. J., & MacCready, P. (2014). The dynamics of pressure and form drag on a sloping headland: Internal waves versus eddies. *Journal of Geophysical Research: Oceans*, *119*(3), 1554-1571. doi: 10.1002/2013JC009757

Washburn, L., Fewings, M. R., Melton, C., & Gotschalk, C. (2011). The propagating response of coastal circulation due to wind relaxations along the central california coast. *Journal of Geophysical Research: Oceans*, *116*(C12). doi: 10.1029/2011JC007502

Wolanski, E., Imberger, J., & Heron, M. L. (1984). Island wakes in shallow coastal waters. *Journal of Geophysical Research: Oceans*, *89*(C6), 10553-10569. doi: 10.1029/JC089iC06p10553

Zeiden, K. L., Rudnick, D. L., & MacKinnon, J. A. (2019). Glider observations of a mesoscale oceanic island wake. *Journal of Physical Oceanography*, *49*(9), 2217-2235. doi: 10.1175/JPO-D-18-0233.1